Theor Chem Acc (2007) 117:847–884
DOI 10.1007/s00214-006-0208-z

REGULAR ARTICLE

Chemical insight into electron density and wave functions: software developments and applications to crystals, molecular complexes and materials science

Luca Bertini · Fausto Cargnoni · Carlo Gatti

Received: 15 June 2006 / Accepted: 13 October 2006 / Published online: 9 January 2007

Abstract This paper overviews the work made by our group during the past 10–15 years on crystalline systems, semiconductor surfaces, molecular complexes and on materials of interest for technological applications, such as the defective silicon or the novel generation thermoelectric materials. Our main aim of extracting chemical insight into the analysis of electron densities and computed wave functions is illustrated through a number of examples. The recently proposed Source Function analysis is reviewed and a few of its more interesting applications are summarized. Software package developments, motivated by the need of a direct comparison with experiment or by the help these packages can provide for interpreting complex experimental outcomes, are described and future directions outlined. A particular emphasis is given to the TOPOND and TOPXD programs, which enable one to analyze theoretical and experimental crystalline densities using the rigorous framework of the Quantum Theory of Atoms in Molecules, due to Bader.

Keywords Electron densities · Quantum theory of atoms in molecules and crystals · Hydrogen-bonded systems · Semiconductor surfaces · Thermoelectric materials · Source function

L. Bertini
Dipartimento di Biotecnologie e Bioscienze,
Università di Milano-Bicocca, Piazza della Scienza 2,
20126 Milan, Italy

F. Cargnoni · C. Gatti (✉)
CNR-ISTM, Istituto di Scienze e Tecnologie Molecolari,
c/o Dip. Chimica Fisica ed Elettrochimica,
via Golgi 19, 20133 Milan, Italy
e-mail: c.gatti@istm.cnr.it

1 Genesis, aim and guidelines of our research activities: a general overview

In spite of the broad diversity of the topics we afforded, a common distinctive feature has characterized our efforts during the past 10–15 years. Namely, we have constantly tried to carry out theoretical "experiments" that could compare to or complement the outcomes from emerging new experimental techniques or chemical applications, and we have always focused our main attention on getting a simple, yet rigorous, chemical insight into our calculations, regardless of how complex they could be. A direct comparison of theory to experiment requires that one adopts a common tool of analysis of the obtained results, while removing all the unnecessary methodological differences that would customarily preclude a meaningful assessment [1]. This prompted us to develop software tools for the analysis and/or the evaluation of experimentally detectable observables, like the electron density or the Seebeck coefficient, or to contribute to the proposal of new chemical descriptors, such as the Source Function (SF) [2], also based on a physical and measurable observable.

We may trace the origin of our work back in 1990, when Riccardo Destro and coworkers had obtained in Milano an experimental electron density distribution (EDD) of excellent quality for the zwitterionic amino acid L-alanine, starting from an extensive set of single-crystal X-ray diffracted intensities measured at 23 K [3]. The very low collection temperature makes the thermal diffuse scattering negligible, minimizes the problems associated with the deconvolution of the static charge density from the mean thermal vibrational distribution of the nuclei and allows for the measurements of extensive sets of data, far beyond the limits usually

encountered at room temperature. The L-alanine X-ray data set was thus the ideal candidate for deriving not only the standard difference-density maps of crystallographers, but also the *total* charge density distribution [4]. Experiment and theory were then becoming directly comparable, provided one had adopted an interpretive tool based on the observable that experiment and theory both determine, and regardless of the different tools—pseudoatom multipolar models [5] or Molecular-Orbitals-like models, respectively—used to extract such an observable. Electron density topology and the underlying quantum theory of atoms in molecules (QTAIM) [6] was the proper method to be used. It would have provided a common framework of analysis, which also gives precious chemical insight. In 1992, we thus published a paper [7] on the experimental *versus* theoretical topological properties of charge density distributions in the L-alanine molecule. Gladly, experimental and theoretical distributions showed the same number and type of critical points (CPs) in the density. However, as far as the CP locations and the CP properties (density, Laplacian, density curvatures) are concerned, a very close agreement between theory and experiment was found only for the non-polar C–C bonds, whereas for more polar interactions like C–O and C–N bonds noteworthy discrepancies were observed. The paper focused on the factors influencing the theoretical topologies, such as the basis set quality, the inclusion of electron correlation and of the crystal-field effects (limited to a molecular cluster approach) and compared the corresponding results to those derived from a number of optimum least-squares refined experimental densities or to those obtained from the very crude independent-atom model [5]. This work aroused a considerable interest and Philip Coppens, in a review paper [8] entitled the *Charge Density Analysis at the Turn of the Century*, reckoned our paper as a "pioneering, first systematic topological analysis using both experimental and theoretical results".

We felt however uneasy with the too approximate treatment of the crystal field effects adopted in the theoretical calculations. Indeed, and quite unexpectedly for us at that time, the intramolecular bond critical point (BCP) properties seemed not to have reached convergence despite the use of an apparently reasonable number of molecules in the cluster approach, whereas the intermolecular BCP properties had converged even at the very crude molecular dimer model level. We thus thought it important to have a tool which could enable us to apply QTAIM directly to the periodic wave functions of the crystals. Roberto Dovesi, Cesare Pisani and Carla Roetti at Turin university, along with Vic Saunders and Nick Harrison at Daresbury (UK) were then developing the upcoming 1995 version of their CRYSTAL package [9], which would have included for the first time both RHF and DFT, along with direct SCF capabilities, in a fully periodic code. These were decisive improvements in view of a comparison with the fast increasing quality of the experimental EDDs. The groups in Turin and Daresbury were kind enough to ask to one of us (CG) to join them and other international groups in a Human Capital and Mobility Program of the European Community (EC) aimed at the "*Development and Applications of the Hartree-Fock Method to Materials Science*". Within this program, CG wrote the code TOPOND-96, the first distributed QTAIM implementation for periodic systems in 0 up to 3 dimensions. The following release of the code, TOPOND-98 [10], and its recent updates and planned future improvements are concisely described in Sect. 2.1, whereas Sect. 2.2 reports the main features of TOPXD [11]—the TOPOND interface to the XD multipolar package [12] enabling one to exploit the specific TOPOND capabilities for experimental densities also.

Applications of TOPOND to the realm of molecular organic crystals paved the way to the interpretation and quantitative evaluation of the effect of packing on molecular EDD topologies [13–15] and on other molecular properties, like the molecular dipole moment [13,15,16] or the electric field gradient (EFG) at nuclei [17]. We could also characterize the *nature* and *function* of the CH$\cdots$O intermolecular interactions [14] in a crystal presenting only this kind of intermolecular bonds, whose appreciation as weak, but not negligible, hydrogen bonds (HBs) had for a long time been debated and even denied in the literature [18]. A summary of some of our results is given in Sect. 3.1.

The earlier mentioned discrepancies between experimental and theoretical EDDs topologies did not in general vanish with inclusion of a proper evaluation of the crystal field [19]. The major reason had to reside somewhere else. Through a fruitful cooperation with Philip Coppens and Anatoliy Volkov at SUNY-Buffalo (US), and using CRYSTAL, TOPOND and TOPXD codes in combination, we could demonstrate that it is mostly the limited flexibility of the radial functions used in the multipolar analysis that often bias significantly the topological experimental results [11,20,21]. Indeed, the observed discrepancies are generally found to significantly decrease when the theoretical densities are projected into the multipole densities functions through refinement of the theoretical structure factors [11,20,21].

Owing to its intimate link with the CRYSTAL package, TOPOND can be naturally used to study 2D periodic systems, like a slab cut from a bulk system along a given crystalline face and then either preserved as a clean surface or allowed to be chemisorbed by suitable chemical passivating species. In a 1996 Chemical

Review paper [22] on the semiconductor surface reconstruction, Charles Duke developed the point of view that the "surface regions of tetrahedrally coordinate semiconductors form new 2D compounds whose bonding, constrained by the requirement of epitaxy with the substrate, exhibits properties distinct from either the corresponding bulk solids or molecules based on the same atomic species". Soon afterwards, in 1998, Ian Robinson published a paper [23] on the state-of-the- art of X-ray crystallography of surfaces and interfaces, where he affirmed that, thanks to the forthcoming developments of surface X-ray diffraction (SXRD) crystallography, one could have expected that the "electron density in bonding electrons at surfaces would have become soon accessible". We immediately thought that TOPOND was the right tool to discuss bonding in these "new 2D compounds" and in a way set to be suitably compared with experiment, once the first accurate and extensive data sets would have eventually become available. Issues like the following could with TOPOND be quantitatively addressed: how is the bonding of surface atoms affected? What is a "dangling" bond and how is modified by surface reconstruction? Why does a surface reconstruct? How rapidly do the surface perturbations and the changes in these perturbations that result from the reconstruction or adsorption process decay into the crystal in terms of the properties of the atoms in each of the succeeding layers? What are the charges on the surface atoms in a free surface and in the chemisorbed states? How much electronic charge is transferred and in what direction? What is the atomic origin and nature of the surface "double layer"?, etc. Section 3.2 exemplifies answers to these questions, by presenting new results on the Si(100) clean and H-covered surfaces and by comparing them with our previously published analysis of the Si(111)(2×1) reconstructed surface [24] and of the Si(111)(1×1) clean and H-covered surfaces [25].

During the last decade, we also took part to cooperative projects in materials science. Atomistic modeling lies at the bottom length-scale of the multiscale modeling computational approach to materials science. This ever more successful approach uses an "information passing" operational mode, where simulations of matter at one scale are based on the results of simulations at a lower, more finely detailed, scale. The continuous demand for improved materials, based on completely new chemical entities, or the increasingly reduced size of material functionalities, as for instance required by the semiconductor industry, makes the modeling on the atomistic scale a necessary prerequisite for any real understanding of the materials' potentiality and for any considerate optimization of the materials' performance. Knowledge of how atoms bond to other atoms, how impurities, doping or atomic substitution affect this bonding, and how bonding, cohesion energy, and the ensuing bulk material properties relate among each other is a typical outcome of an atomistic-level simulation. However, bonding in pure or defective solids or in complex supramolecular aggregates cannot often be easily interpreted with standard methods of bond analysis and the use of QTAIM, a method firmly rooted in physics, and not based on any preconception of bonding, has proved to be particularly helpful in this case [1,26].

In cooperation with L. Colombo (INFM, Milano) and within the finalized national CNR project *Innovative materials for advanced technologies*, we addressed the structural and bonding problems related to the migration and interaction of native point defects in silicon, a phenomenon affecting many, industrially relevant, micro- and mesoscopic properties of silicon bulk samples. Section 4.1 reports a brief summary of our study [27] on a kind of bond defects (BDs), arousing from the incomplete recombination of vacancy–interstitial pairs in silicon, and of our interpretation [28] of the structural and energetics evolution which takes place during the growth of self-interstitial clusters in the silicon crystal.

The main emphasis of Sect. 4 is however devoted to illustrating our recent work on thermoelectric (TE) materials within the EC Vth Framework Program European Community project called "*Nanothermel—High performance thermoelectric materials for heat recovery and cooling applications*" [29]. This project, started in year 2001, has involved six academic groups and two industrial partners with quite an interesting blend of fundamental, synthetic, structural, electro technical and technological competences.[1] Nanothermel is aimed at developing nano-engineered high performance TE materials and devices, through a dual strategy, which combines novel chemical methods for fabricating nanophase TE materials with the systematic introduction of structural modifications in new generation host–guest TE materials. Our group has focused on the relationships between the TE material geometrical and electronic structure and its ensuing electronic transport properties. These may be obtained from the knowledge of the full band structure, using the semi-classical Boltz-

[1] Christiansen M and Iversen BB (University of Aarhus, Denmark), Saramat A and Palmqvist A (Chalmers University of Technology, Goteborg, Sweden), Noriega G (CIDETE, Spain), Gatti C and Bertini L (CNR-ISTM, Milano, Italy), Holmgren L (LEGELAB, Sweden), Müller E, Platzek D, Stiewe C (German Aerospace Center (DLR), Institute of Materials Research, Cologne, Germany), Rowe DM and Williams SG (NEDO—Laboratory for Thermoelectric Engineering, Cardiff, UK); Toprak M, Zhang Y, Muhammed M (Royal Institute of Technology, Materials Chemistry Division, Stockholm, Sweden).

man's transport theory and the approximation of a constant relaxation time [30–32]. A code, named ELTRAP (Electron Transport Properties), and interfaced to the CRYSTAL-98 package [33] has been developed by us [34], as briefly illustrated in Sect. 2.3. Given a newly synthesized TE material of known starting stoichiometry, it is very difficult, if not often impossible, to know its precise geometrical structure, not to speak of its exact composition. Furthermore, its TE properties are typically the result of the combined effect of the different geometrical structures and/or chemical local compositions characterizing the material. Ab initio theoretical modeling may produce several useful feedbacks. For instance, we have been able to show that the Seebeck coefficient and its trend with the temperature or with the doping level is a very precious structural informer [35]. More in general, theoretical modeling singles out the effects that a well-defined composition and general structure has on the geometrical, electronic and TE properties and it so allows for a rational design of improved performance materials [36]. Theoretical modeling also provides a synergic help and a mutual validation between computed and multi-techniques experimental structural hypotheses, as testified by the fruitful cooperation [37–40] we had with the structural group at Aarhus University (DK), headed by Bo Iversen. Finally, ab-initio modeling can be used as a guidance for design of optimum TE materials through the prediction of the best doping level based on the computed electronic transport properties. A number of published [37–40] case studies on new generation TE materials, like the type I Inorganic Clathrates $A_8Ga_{16}Ge_{30}$ (A=Sr, Ba), the Zn–Sb alloys and the modified Co_4Sb_{12} skutterudite phases are illustrated in Sect. 4.2, along with the work currently in progress.

We put an end to this introductory overview by mentioning our recent work on the SF, first proposed by Richard Bader and by one of us (CG) in 1998 [2]. This function enables one to equate the value of the density at any point within a system to a sum of atomic contributions and to thus view properties of the density from a totally new perspective. Although not deliberately put forward for such a purpose [2], the SF permits to get through one of the most debated aspects of QTAIM [1,41–44] one which is customarily considered as an intrinsic limit of the theory [45,46]. Within QTAIM, a bonding interaction between two atoms is associated to the presence of a line of maximum density, that is a bond path (BP), linking their nuclei at electrostatic equilibrium [47]. However, a BP is topologically associated to the only two atoms it connects and it is thus inherently unable to directly visualize an interaction involving more than two centres, despite both the BP occurrence and its shape depend in principle on the whole set of physical interactions present within a system. The SF unveils such a dependence, by pointing out which other atoms, besides the two connected by the BP, significantly contribute to the observed density accumulation along the path and, in particular, at the BCP. Other bonding descriptors, like the QTAIM delocalization index [48] or the synaptic order of an ELF valence basin [45,49] give access to *non-local* information on bonding and on complex, unconventional bonding patterns. A distinctive feature of the SF with respect to these two powerful interpretive tools is that it is directly amenable to experimental determination, as due to its intimate link with the system's electron density Laplacian. This puts the SF in a privileged position for retrieving comparative bond information from experimental and theoretical results. A concise mathematical introduction to the SF is given in Sect. 5.1, while Sect. 5.2 reports a summary of our recent SF applications on H-bonded complexes [50,51] and on *d*-block organometallic compounds [52]. An outlook to the current and future developments of the SF concludes Sect. 5.

2 Chemical insight into electron density and wave functions: software developments

The general motivations behind the development of TOPOND, TOPXD and ELTRAP codes have been summarized above. This section briefly outlines the main functions and specific features of these codes.

2.1 TOPOND: a code implementing QTAIM for periodic systems

As due to its interface with the libraries of and the output from the CRYSTAL package, TOPOND [10,13,53] considerably differs from the other existing implementations of QTAIM for crystalline systems (see Refs. [54,55] for a not exhaustive list). Indeed, in most codes, the electron density is analyzed in a user's defined volume, which normally is chosen so as to include the basin of the unique atoms of the system and the basins of their bonded atoms. The periodic nature of the system is not exploited, and the topological study of the electron density in the crystal becomes essentially that of the density of a large cluster of atoms extracted from the crystal. The electron density is either calculated analytically, using only contributions from the atoms in the cluster, or simply given on a grid. The electron density derivatives, which are required up to the second order for the topological analysis of $\rho(\mathbf{r})$ and up to the fourth order for that of $\nabla^2\rho(\mathbf{r})$, are usually not available in analytic form and

are therefore estimated through numerical procedures, especially those with order greater than 2. Although both needed in principle for a full implementation of the QTAIM analysis, the one-electron density matrix (ODM) and the pair density are also not accessible, in general, in the other codes.

Save for the availability of the pair density, every one of the listed weaknesses are overcome in TOPOND. This code takes advantage of the full-periodic machinery of the CRYSTAL package, of its libraries for the analytical density derivatives up to the fourth order and of its easy accessibility to the ODMs associated to orbitals located either in the same reference cell or in different crystal cells. CRYSTAL treats systems with different dimensional periodicities (0, molecules, 1 polymers, 2 slabs and 3, crystals) on an equal footing, with the single particle wave functions being expanded as a linear combination of Bloch's functions, for any periodicity beyond zero. Since the 230 space groups, 80 layer groups, 99 rod groups and 45 point groups are all available in CRYSTAL, TOPOND is, by design, a powerful tool for applying QTAIM to molecules, polymers, surfaces and crystals using a single code and exploiting the full symmetry of every of these systems. It does so working on electron densities obtained with a similar accuracy for different aggregations of matter and using the same kind of algorithms to topologically analyze their corresponding densities. Since ODMs are available, TOPOND evaluates exactly typical QTAIM descriptors like the kinetic energy densities $K(\mathbf{r})$ or $G(\mathbf{r})$, the virial density $V(\mathbf{r})$, or also the electron localization function (ELF) due to Becke [56], without resorting to their approximate expressions [57] in terms of $\rho(\mathbf{r})$, $\nabla\rho(\mathbf{r})$ and $\nabla^2\rho(\mathbf{r})$ as other topological codes for periodic systems necessarily do.

In the presently distributed TOPOND-98 version [10] (http://www.istm.cnr.it/~gatti/TOPOND.ppt), the TOPOND package includes sections implementing a full topological analysis of $\rho(\mathbf{r})$ and of $\nabla^2\rho(\mathbf{r})$ scalar fields. Two different CP search algorithms are available to the user. One is the Newton–Raphson (NR) technique, the other is the more refined eigenvector following (EF) method proposed by Popelier [58]. This latter approach is akin to the NR method, but it uses, at each stage of the CP search, a suitable and locally defined shift for the conventional NR step, a shift which depends on the actual nature—minimum, 1D or 2D saddle point, maximum—of the CP one is looking for. This makes the EF method able to seek for the CPs of a given kind regardless of the structure of the Hessian the scalar field has at the starting search point, and thus much less sensitive to the choice of good starting search points than is the NR algorithm. The EF is the method of choice for the topological study of $\nabla^2\rho$ as this scalar function may vary extremely rapidly, especially in those valence regions which are of greatest chemical interest. Separate searches for the different kinds $(3,-3;3,-1;3,+1,3,+3)$ of CPs are implemented for both fields, whereas for $\rho(\mathbf{r})$, also a fully automatic search strategy, able to locate one after the other all kinds of CPs, is offered. The automatic procedure adopts the relevant EF step prescription for each kind of CP searched for in sequence. First, $(3,-3)$ maxima associated to nuclei are located, then $(3,-1)$ BCPs are searched for between all the unique pairs of a set of nuclei, where the set is assembled by building up clusters of atoms of given radius around each unique atom in the unit cell or by constructing a cluster of atoms around a selected seed point in the crystal. Non-nuclear $(3,-3)$ attractors (NNA) [6,59], i.e., electron density maximums which are not associated to nuclei, are then also recovered at this stage, if any are present in the crystalline density. NNAs are discerned by determining the termini of the BPs associated to each of the unique $(3,-1)$ CP found and by checking whether the fractional coordinates of these termini are consistent or not with the Wickoff positions [60] of the atomic species present in the crystal. Afterwards, $(3,+1)$ ring CP searches are launched by examining all the triplets of nuclei having at least two of their nuclei bonded to each other and a center of mass not too differently distant from each nucleus in the triplet (all nuclei have a mass equal to one for the purpose of this calculation). Finally, $(3,+3)$ CPs are searched for between all pairs of ring CPs. The automatic procedure has proved to be able to recover most of the relevant intra- and intermolecular interactions present in a molecular organic crystal. Information on the crystal periodicity is never lost at each stage of the procedure, even when the code is apparently working on a selected number of atoms. For instance, all atoms equivalent for symmetry are always easily recognized and unnecessary calculations avoided. When a CP is located, a full list of neighboring atoms, with their exact cell locations and coordinates given either in fractional or Cartesian form is immediately accessible.

A CP search on a grid, defined in the asymmetric unit, is also available to the user for those special cases where the Morse topological relationship [61], given by Eq. 1,

$$n - b + r - c = 0 \tag{1}$$

and where n, b, r and c are the total number of nuclear, bond, ring and cage CPs, is not fulfilled by the set of CPs found using the fully automatic search. The CP search on a grid turns out to be from two to up to three order of magnitude computationally more expensive than the automatic search [53], but it hardly ever misses CPs, even

for the very flat density distributions typically found in metals. Atomic interaction lines (BPs, ρ field) and atomic graphs ($\nabla^2\rho$ field) are determined by TOPOND by tracing the associated steepest ascent/descent $\nabla\rho$ or $\nabla(\nabla^2\rho)$ paths, using a fifth-order Runge–Kutta method with monitoring of local truncation error and an adaptive step-size control [62]. Typically 80–100 integrations steps for a total of about 500–1,000 evaluations of the function and its first derivative are required for each line. The parameterization of the implemented algorithms required special care in order to obtain correct atomic interaction lines also in the case of metals, which are known to have a rather complex and often unstable network of interaction lines [53,63,64]. Apart from the general flatness of the metal valence electron distributions [65], this is also due to the frequent occurrence of NNAs [63–65], whose location and number is easily modified by small changes in the computational model (e.g., basis set) or in the cell parameters, as caused by a variation in the external pressure. Luaña et al. [63,66] identified as many as ten different topologies for Li bcc using a FPLAPW/GGA approach in a 0.5-Å interval around the experimental lattice parameter at normal pressure, and a distinct topology for each of the four different computational methods they scrutinized at the experimental geometry.

Another section of TOPOND deals with the evaluation of the atomic basin boundaries, as defined by the condition of zero flux of $\nabla\rho$ at each point of the boundary. Within the portions of crystal space so defined, the same section of TOPOND computes several physical quantities, hereinafter referred to as *atomic properties* [6]. These include the atomic net charge, the atomic kinetic energy, which corresponds to minus the atomic energy for a system at electrostatic equilibrium, the atomic dipole, giving the displacement of the centroid of the electronic charge from the nucleus, the atomic quadrupole, expressing the departure of the atom's electron distribution from spherical symmetry, the atomic volume, the atomic Shannon information entropy [67], and so on and so forth. The evaluation of interatomic surfaces uses an indirect, time consuming, algorithm due to Keith [13,68], whereas the integration of properties within the atomic boundaries is performed via a Gauss–Legendre quadrature approach [62] using accurate grids in spherical coordinates (typically 3,000 angular points and about 150 radial points for each angular point). The integration is generally very accurate. For instance, in urea, the computed total molecular volume—as obtained by summing up the volumes of the atoms of a molecule in the crystal—differs by less than 0.2% from the volume per molecule in the unit cell and the corresponding sum of the net atomic charges differs from zero by less than 0.005e [13]. This kind of accuracy is required for a precise evaluation of the molecular dipole moment enhancement upon crystallization [11,13,15,16]. Such a dipole increase may be noticeable, even as large as 70%, but hardly visibly detectable if one simply compares the EDD of the crystal and that resulting from the superposition of the density of isolated molecules placed at the same positions as in the crystal [26].

A last section of TOPOND performs the grid evaluation of several scalar fields, including the electron density and spin density, the electron density Laplacian, the magnitude of $\nabla\rho$, the kinetic energy densities G and K, the virial density V, the ELF and its α and β components. Molecular/crystal graphs [1,6], or generically, $\nabla\rho$ trajectories are also traced out in selected molecular/surface/crystal planes. Gradient paths, which emanate from 3D or 2D attractors lying on the plot plane but not within the plot boundaries, are also calculated so as to obtain a complete display of the $\nabla\rho$ trajectories in the selected plot area. This section of TOPOND is interfaced to the program P2DCRY97 [69], which produces graphical representations (HPGL format) of the contour plots of all the computed scalar functions or of their differences, optionally overlaid by $\nabla\rho$ trajectories as selected by the user (e.g., a contour plot of the electron density overlaid by the $\nabla\rho$ trajectories which denote the intersection of the atomic surfaces with the plane of the plot).

Along with Philippe Rabiller in Rennes (France), we have recently compared [55] the performance of TOPOND-98 to that of InteGriTy [54], a code performing a topological analysis of the electron density sampled on 3D grids, using as a simple test the crystal of urea and the electron density calculated by the CRYSTAL code. Mesh sizes as small as 0.025 Å are needed in InteGriTy to provide well-converged local and integrated results when the valence and core electron densities are not treated separately [55]. Using this mesh size, analytical (TOPOND-98) and numerical (InteGriTy) results showed a very good overall agreement both for the BCP properties and those integrated properties which can be calculated from the electron density alone. In the case of the basin surface determination and basin integration, the computing time is clearly in favor of the InteGriTy code, but when the time needed to build the grid is also taken into account, the two methods become comparable. Obviously, InteGriTy is the package of choice when the density is only known on a grid, as is the case of densities derived from the maximum entropy method applied to X-ray diffraction data [38,70]. When both the density and its derivatives can be calculated analytically and the wave function is also obtainable, TOPOND is clearly superior. Not only the full information related

to the crystal periodicity is directly accessible, but all the properties derived from the ODM are also available, with the further advantage that these properties, including the set common to the InteGriTy package, are computed as "exact" analytical values. In addition, performing a topological analysis of $\nabla^2\rho$ with InteGriTy is very troublesome, if not impossible, unless one may adopt extremely small, and thus computationally expensive, mesh sizes.

TOPOND-98, interfaced to CRYSTAL-98 [33], has so far been distributed in over 50 international laboratories active in the field of crystallography, solid state physics, physical and theoretical chemistry, inorganic chemistry, geology and mineralogy, etc. A necessary interface and several improvements of the code are planned for the near future. First of all, work is in progress to interface TOPOND with the most recent release of the CRYSTAL code [71]. Secondly, the section on the evaluation of the interatomic surface properties is currently being implemented. Properties will include, among the other, the integrated surface charge [6], the external SF contribution to the density within an atomic basin [2] (see Sect. 5.1) and the net flux of the total electric field, yielding, through the Gauss theorem [72], the net charge of an atom and the separate contributions to this quantity from the groups of atoms linked to a given atomic basin. Third, we plan to introduce the computation of the "exchange part" of the second-order density matrix [73], so as to evaluate the Fermi Hole [6] and the ensuing localization/delocalization indices [48] for Hartree-Fock (HF) or Kohn–Sham type crystalline wave functions. Finally, work is in progress to implement a rigorous full population analysis, based only on the $\rho(\mathbf{r})$ observable, and making use of the SF formalism (see Sect. 5.3).

2.2 TOPXD: a code implementing QTAIM for electron density distributions from X-ray data

Over the past decade, QTAIM has increasingly been applied to crystalline systems [1,74], in particular to the electron densities derived from experiment, and nowadays QTAIM is no doubt the primary standard theory adopted by the X-ray community to discuss bonding in crystals. There are two main reasons behind this choice.

First, several technical progresses have made X-ray diffraction a unique tool for mapping the charge density in crystals in these years [74,75]. Progresses include the accessibility to intense short-wavelength synchrotron sources, the availability of commercial devices for low-T collections, the advent of area detectors, which have all led to a noteworthy increase of the attained X-ray data quality, even for the difficult cases like the compounds containing heavy elements—the heavier the element, the smaller the fraction of scattering stemming from the valence electrons relative to the core contribution—or the crystals with highly symmetric structures and hence very few Bragg's reflections in the low-order region where valence scattering is concentrated [75].

Second, the noteworthy advances in the ab initio periodic approaches [76,77] which now enable one to calculate reliable electron densities for crystals having even a large number of atoms (>50–100) in the unit cell, that is for those large systems normally investigated by the X-ray density crystallographers. As mentioned in Sect. 1, QTAIM is then the theory of choice for an unbiased comparison between theoretical and static experimental densities [1,74,78] and theory and experiment may pleasingly complement each other. Comparison of their outcomes may provide useful information on the quality of experimental data, the suitability of the multipolar model used to project the reciprocal space representation of ρ to its real-space counterpart [7,20]. Or, in the case of theory, a comparison with experiment may, for instance, reveal how important is the lack of an adequate treatment of correlation—in particular of the dispersion forces—or how influential is the choice of a certain basis set [7,20] or of a given number of active electrons in a pseudopotential approach [79].

Not surprisingly, a number of codes implementing QTAIM for experimental crystalline densities have thus appeared in the last decade, one of which is TOPXD [12] (http://harker.chem.buffalo.edu/public/topxd/). This code, developed in cooperation with Volkov and Coppens at SUNY-Buffalo (US), allows for a complete topological analysis of experimental charge densities, expressed in terms of the Hansen–Coppens multipole formalism [5]. It is essentially based on TOPOND-98, except for the subroutines for geometrical calculation and density evaluations which have been rewritten according to the XD package convention, with XD [12] (http://xd.chem.buffalo.edu/intro.html) being the most widely distributed program for the experimental charge density multipole refinement. TOPXD has now become fully integrated in the most recent version of XD [12]. The main features of TOPXD are those of its parent code, although it contains important improvements and unavoidable limitations compared to TOPOND. It is more documented, has a friendly input style, increased speed in evaluating the interatomic surfaces and added facilities for their 3D visualization. However, the ODM is not available within TOPXD and no property depending from this matrix can be evaluated. The experimental electron density and its derivatives are calculated analytically only up to order 2, using subroutines from

the XD package. Higher derivatives (third and fourth order) are only estimated numerically and obtained from a finite-difference approximation of the first- and second-order analytical derivatives [11]. The accuracy of the numerical differentiation of the electron density has been extensively tested by comparing the numerical first and pure second derivatives with those obtained analytically in a number of selected points in the crystal of *p*-nitroaniline (PNA) [11]. Errors as low as 1×10^{-9} au, using single precision, and practically zero, using double precision variables, were observed for a step size of 5×10^{-3} au. The actual remaining drawback is the need of evaluating the density at several points (e.g., five for a pure second derivative) in order to obtain the numerical estimate of each density derivative. More details can be found in the original paper [11], along with interesting comparisons between the atomic properties of PNA, calculated by TOPOND or TOPXD and using either electron densities from theory (TOPOND) or both from theory and experiment (TOPXD). Analysis of the differences between the TOPOND results and those obtained by TOPXD when simulated X-ray diffraction data derived from the theoretical structure factors are input to this code, allows for a direct estimate of the bias on the bond and the atomic properties introduced by the adopted multipolar model [11,20].

2.3 ELTRAP: a code for evaluating electron transport properties

As mentioned earlier in Sect. 1, our participation to the Nanothermel project led us to develop a code, named ELTRAP, for the estimation of the electronic transport properties, using the semi-classical Boltzmann's transport theory [30,31] in a monoelectronic formulation and in the approximation of a constant relaxation time [31, 32]. ELTRAP is interfaced to CRYSTAL-98, which calculates the electronic structure of a crystalline material and provides to ELTRAP the full information on its band structure. The electronic transport properties σ, $\boldsymbol{S}$ and κ_e (electrical conductivity, the Seebeck coefficient and electronic contribution to the thermal conductivity) are all second-rank tensors and are derived from the expression of the Onsager coefficients $\mathbf{L}_\mathrm{i}$,

$$\mathbf{L}_i = 2\sum_n \int_{1\mathrm{BZ}} \tau_n(\mathbf{k},T)v_n^2(\mathbf{k})(\mathrm{E}_n(\mathbf{k})-\mu)^i \times\left(-\frac{\partial f_0}{\partial\varepsilon}\right)_{\varepsilon=E_n(\mathbf{k})} \mathrm{d}\mathbf{k}, \quad i=0,1,2 \tag{2}$$

The integral in **k**-space is over the first Brillouin zone (1BZ), $\tau_n(\mathbf{k},T)$ is the relaxation time, $E_n(\mathbf{k})$ and $v_n(\mathbf{k}) = (1/\hbar)\partial\mathrm{E}_\mathrm{n}(\mathbf{k})/\partial\mathbf{k}$ are the nth band energy and velocity, respectively, as a function of **k**, and f_0 is the Fermi–Dirac distribution function [31]. The chemical potential μ is derived, for any given temperature T, from the equivalence given in Eq. 3,

$$N_\mathrm{e}N_\mathbf{k} = \sum_{n,\mathbf{k}} \frac{2}{1+e^{[E_n(\mathbf{k})-\mu]/(k_\mathrm{B}T)}} \tag{3}$$

where N_e and $N_\mathbf{k}$ are the number of electrons in the cell and the number of **k** points sampling each band, respectively. If the relaxation time τ is assumed to be constant and independent of **k**, n and T, one can easily obtain the transport properties $\boldsymbol{\sigma}$, $\boldsymbol{S}$ and $\boldsymbol{\kappa}_\mathrm{e}$ from the $\mathbf{L}_i$ coefficients:

$$\begin{aligned}\boldsymbol{\sigma} &= e^2\tau\mathbf{L}_0\\ \mathbf{S} &= \frac{1}{eT}\mathbf{L}_0^{-1}\mathbf{L}_1\\ \boldsymbol{\kappa}_e &= \frac{\tau}{T}\left(\mathbf{L}_2-\mathbf{L}_1\mathbf{L}_0^{-1}\mathbf{L}_1\right)\end{aligned} \tag{4}$$

It is worth noting that $\boldsymbol{S}$ turns out to be τ independent within this approximation.[2] ELTRAP evaluates numerically the integrals in Eq. 2 by sampling the band structure $E_n(\mathbf{k})$ on a equally spaced cubic grid. For $CoSb_3$ and its structural modifications, we used equally spaced cubic grids with typically 40^3 k-points per band and a total of about 20 bands, 10 below and 10 above the Fermi level. The $E_n(\mathbf{k})$ values are read from FORT.25 CRYSTAL output file and the band velocities are computed through a cubic spline interpolation [62].

Measured S values for semiconductors are very sensitive to carrier's concentration. One may thus combine Eqs. 2 and 3 and try to reproduce these values by tuning the carrier's concentration within the frozen band approach. More interestingly, use of the frozen band approach and of a variable non-integer number of electrons in Eq. 3 allows for an estimate of the amount of doping which would maximize the performance of a given material. For instance, in the case of TE materials, we have estimated the optimal doping level as the one yielding maximum power factor $S^2\sigma$ [35,36]. Maximizing $S^2\sigma$ permits to find out the most favorable TE doping at a given T, in the hypothetical case of the lattice component of the thermal conductivity largely exceeding the electronic one (see Sect. 4.2).

[2] In Sect. 4.2, the isotropic parts σ, κ_e and S of the computed tensors, given as 1/3 of their traces, are reported.

3 Applications to crystals and surfaces

The chemical insight we gained by applying QTAIM to molecular crystals and silicon surfaces is reviewed below.

3.1 Molecular crystals

Electron density distributions of molecular crystals are an incredible source of information on the weaker and more unusual atomic interactions, besides that on conventional gas-phase chemical bonds [1]. Molecular crystals are typically characterized by the concomitant presence of usually strong, intramolecular bonds, and of normally weak, intermolecular contacts, and with the properties of both kinds of interactions being reciprocally influenced relative to the isolated molecule or to a small aggregate of molecules (dimer, trimer). During the past decade, QTAIM has proved to be a useful tool to single out and characterize the weak intermolecular interactions responsible for molecular crystal formation, and to give a quantitative measure of how the onset of these interactions affects the intramolecular bond properties [1]. Our pioneering work [13] on the urea crystal represents an exemplar application of QTAIM and TOPOND to the study of such effects—an extensive and didactic account of which can be found for urea in Ref. [26]. Here, we just summarize a few results. Upon crystallization, we found changes from 0 up to 3% for ρ_b, the value of the electron density at BCPs, and even up to 40–60% for $\nabla^2\rho_b$ and λ_{3b}, the values of the Laplacian of the density and of the positive density curvature along the BP, also measured at BCPs.[3] Clearly, being related to second derivatives of the electron density, $\nabla^2\rho_b$ and λ_{3b} are more sensitive indicators of crystal field effects than is ρ_b or other bond topological properties which are not mentioned here. More importantly, all the observed changes could be easily and convincingly rationalized in terms of an enhanced ionicity or covalency of the intramolecular bonds as caused by the formation of the HBs in the crystal. For this purpose, we analyzed the direction and magnitude of changes of the bond topological indicators typically associated to the dicothomous classification [1,80] of atomic interactions based on the sign of $\nabla^2\rho$ at BCP. We could also rationalize an interesting anomaly of the urea structure, that is that of providing the only known instance of a carbonyl atom which accepts four N–H$\cdots$O HBs [81]. Indeed, the considerable lengthening of the C–O bond occurring in the crystal (from 1.229 to 1.261 Å) modifies the Laplacian distribution of the oxygen atom by forming a torus of nearly uniform charge concentration in its non-bonded regions, a fact which promotes its involvement in four HBs (two with another coplanar urea molecule and the other two with urea molecules lying in adjacent perpendicular planes). Application of QTAIM to condensed phases allows for a clear definition [13,15,16] of the molecular dipole $\boldsymbol{\mu}$ in the crystal and of its charge transfer, $\boldsymbol{\mu}_{CT}$, and atomic polarization, $\boldsymbol{\mu}_{A}$,components [82]. Upon crystallization, the H atoms in urea become more positively charged, whereas all heavy atoms have their population increased, the net result being a more polarized molecule, an enhanced dipole moment magnitude, and a flux in the crystal of 0.066 electrons from each amino-group hydrogen donor to the carbonyl group acceptor. The molecular dipole moment magnitude $|\boldsymbol{\mu}|$ increases in the crystal by 37 and 53% relative to the isolated molecules at crystal and optimized geometry (OG), respectively. The large dipole moment increase in the bulk is primarily the result of a large increase of the magnitude of the charge transfer component $\boldsymbol{\mu}_{CT}$, which contributes to about 88 and 73% of the reported enhancements. A corresponding analysis [16] on ice VIII and on a number of prototypical structures of ice also led to a similar picture. The calculated molecular dipole moment increase of water induced by crystallization was found to be rather sensitive to the structure and lying in the range 0.1–0.6 D. These results provided realistic estimates of the water effective dipole moment in condensed phase.

In the following, we review in some detail a recent and more complex application [14,15] of QTAIM to molecular crystals. It deals with the interesting problem of the nature and function of the weak CH$\cdots$O intermolecular interactions, through the analysis of the experimental and theoretical densities of the 3,4-Bis(dimethylamino)-3-cyclobutene-1,2-dione (DMACB) crystal. This system, characterized by several intermolecular and intramolecular CH$\cdots$O interactions, represents a particularly appropriate test case for studying this kind of weak interactions in a crystal, since no other type of stronger, and thus successfully competing HB, is present. We have asked ourselves a few basic questions: (a) does the existence or the absence of an H–O CP reflect specific geometrical features of a CH$\cdots$O contact in the DMACB crystal? (b) Can the bonded CH$\cdots$O contacts in this crystal be classified as true HB? (c) Do the crystal and procrystal densities differ in the topological features of their CH$\cdots$O contacts and can the CH$\cdots$O bond energies be thus reliably retrieved from the BCP properties alone? (d) Do the weak intermolecular HBs induce a large molecular dipole moment enhancement upon crystallization as typically found in molecular crystals tied by the much stronger NH$\cdots$O

[3] From now on, the subscript b denotes a QTAIM topological property evaluated at a BCP.

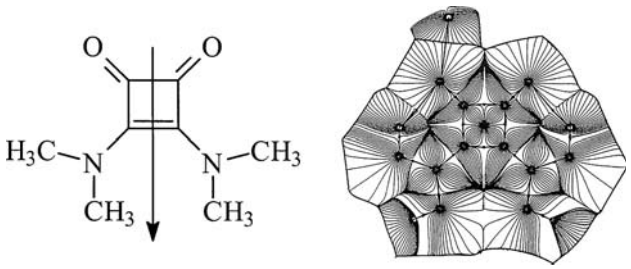

Fig. 1 3,4-Bis(dimethylamino)-3-cyclobutene-1,2-dione (DMACB). *Left* scheme of the gas phase molecule (C_2 symmetry). The dipole moment is directed along the C_2 axis. *Right* Molecular graph and $\nabla\rho$ trajectories for a DMACB molecule in the crystal. The molecule adopts in the bulk a nearly coplanar conformation for all non-H atoms. The bond paths related to the two intramolecular CH···O HBs between each keto-oxygen and the facing methyl-H atom are clearly visible. An intermolecular CH···O bond is shown in the top-left part of the figure (Reprinted from Fig. 4 with permission from Ref. [15], Copyright 2001 American Chemical Society)

and OH···O bonds? Answers to these questions are provided below.

3.1.1 The 3,4-Bis(dimethylamino)-3-cyclobutene−1, 2-dione crystal

The DMACB molecule (Fig. 1) has a C_2 symmetry gas-phase conformation, with $C_{ring} - C_{ring} - N - C_{methyl}$ torsion angles of about 40°, and a large dipole moment of about 2.8 au, directed along the rotation axis [83]. The molecule adopts in the solid a nearly coplanar conformation for all non-H atoms (Fig. 1) and crystallizes in the triclinic $P\bar{1}$ space group, below 147 K [84]. In the triclinic structure, there are two crystallographic independent types of molecules (named as *A* and *B* in the following), each type forming columns of stacked molecules with a head-to-tail arrangement of their molecular dipole moments. This molecular packing entails 23 unique inter- and intra-column CH···O contacts, for H···O distances ($d_{H\cdots O}$) below 3.0 Å [14]. The contacts span a range of distances (2.351Å $< d_{H\cdots O} <$ 2.969 Å), whose confines are close to or well above the "restrictive" 2.4 Å threshold for potential CH···O bonds [85, 86]. In addition to the intermolecular contacts, there are four unique intramolecular CH···O short (2.211 Å $< d_{H\cdots O} <$2.248) interactions—two for each type of molecule—between the keto-oxygen and its facing methyl-H atom (Fig. 1), leading to a total of 27 unique CH···O contacts in the crystal.

The *nature* of the CH···O interactions has been amply discussed in the past 70 years [18,86]. For instance, the debate on the angular preferences, or lack thereof, of the weakest kinds of CH···O interactions is intimately tied to their very nature of either directional true HBs or of non-directional van der Waals-like interactions. As for their *role*, the CH···O contacts do not only represent a non-negligible energetic contribution to the packing energy on their own, but also, if able to cause a significant molecular dipole moment increase upon crystallization—as demonstrated below, see sect. 3.1.4 — they can have an even more important impact on the packing energy [14]. Indeed, the adoption of a molecule planar conformation in the DMACB crystal allows for an increase of the energetic weight of the attracting dipole–dipole interactions arising from the head-to-tail arrangement of the molecular dipole moments along each column. Then, if the molecular dipole is enhanced upon packing, such an enhancement sums up to the geometrical effect in determining an increase of the dipole–dipole contribution to the interaction energy [14,15].

3.1.2 Nature of CH···O interactions

Figure 2 shows the $C\hat{H}O$ (α_{CHO}) angular distribution *versus* the H···O separation, $d_{H\cdots O}$, for the 27 unique CH···O contacts considered. Using the BP criterion for distinguishing the bonded from the non-bonded contacts, one observes that 23 out of 27 contacts are *bonded* and characterized by a large and approximately constant (120°–140°) α_{CHO} value. Conversely, all the four contacts found *non-bonded* have a much more bent geometry, with α_{CHO} values close to or even below 90°. Interestingly, the $C\hat{H}O$ angular distribution observed for H···O separations greater than 2.7 Å is only apparently isotropic, since this feature is abruptly removed if the angular distributions of the bonded and non-bonded contacts are separately analyzed. Thus, the BP criterion, when applied to the CH···O contacts in the DMACB crystal, is able to single out the contacts characterized by an important contribution of the monopole–dipole and dipole–dipole interaction from those which may be better classified as van der Waals' like non-bonded contacts.[4]

We then asked ourselves whether all the identified CH···O bonded contacts could be classified as "genuine" HBs. To address this point, we applied to the condensed phase for the first time [14] the full set of criteria previously proposed by Koch and Popelier [87] to establish and characterize HBs in the gas phase. Besides requiring the presence of a CP with characteristic topological features, the criteria comprise the mutual

[4] Electrostatic interactions favor a linear or a close to linear geometry over a bent one, whereas the van der Waals' type contacts do not have an energy angular dependency and the α_{CHO} angle may be so even folded down below 90°.

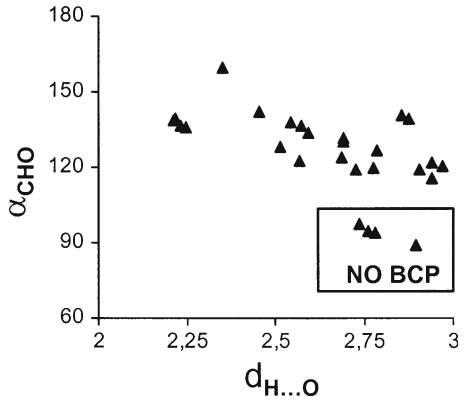

Fig. 2 C $\hat{H}$ O angles (α_{CHO}) *vs* $d_{H\cdots O}$ distances (Å) for CH$\cdots$O contacts in DMACB crystal. Enclosed in a *box* are the *non-bonded* CH$\cdots$O contacts, that is those contacts lacking a BCP. If the non-bonded contacts are identified and separately analyzed, the CH$\cdots$O bonds retain a *non-isotropic* angular distribution even beyond $d_{H\cdots O} > 2.7$ Å

penetration[5] of the hydrogen and the acceptor atoms and the occurrence of a number of changes in the integral properties of the H atom following H-bond formation: a decrease of the H electron population, atomic moment and volume, accompanied by an increase of its atomic energy.

Importantly, all the mentioned criteria were found to be fulfilled by the whole set of intermolecular CH$\cdots$O bonded contacts, with just one outlier out of a 114 values data set (6 criteria times 19 intermolecular unique H-bonds). In particular, the sufficient criterion of a mutual H and O penetration was neatly satisfied by all interactions, with the H-atom penetrations generally decreasing with increasing HB length within each group of intercolumn or intracolumn HBs. Therefore, the H-atom forming a bifurcated intercolumn HB turned out to be more penetrated ($\Delta R = -0.148$ au) in the direction of the shorter ($d_{H\cdots O} = 2.907$ Å) and stronger than it is ($\Delta R = -0.122$ au) along the longer and weaker ($d_{H\cdots O} = 2.942$ Å) of the two HB it forms. Much greater H penetrations ($|\Delta R| \approx 0.3 - 0.4$ au) were found for the shortest CH$\cdots$O interactions. The subset of criteria[6] applicable to an experimental electron density was also satisfactorily fulfilled by the DMACB experimental density.

[5] Penetration is measured by the difference ΔR between the non-bonded radius of the H or of the O in the isolated molecule and the distance from the corresponding atoms to the HB CP in the crystal. The non-bonded radius is taken as the average distance from the nucleus to the 0.001 au contour in the isolated molecule [6].

[6] This subset include: the existence of the HB CP with characteristic features, and the changes of the H atomic properties except for the H atomic energy.

The case of the four intramolecular CH$\cdots$O interactions, which are already present in the isolated DMACB molecule, provided, on the other hand, a test case for a *differential* application [14] of Koch and Popelier criteria. Rather than considering changes in atomic properties and atomic penetrations due to H-bond formation, we analyzed in this case how these quantities change because in the crystal the O atoms become also simultaneously involved in the HB intermolecular interactions. The observed variations can therefore occur in either directions and we reasonably assumed that if the changes taking place in the crystal for the intramolecular interactions have a reverse direction compared to that expected upon H-bonding, then the intramolecular HBs have likely been weakened by the simultaneous formation of the intermolecular HB network. Indeed, upon crystal formation, the H atoms involved in the intramolecular HBs increase, instead of decreasing, their electron population and volume, and decrease, rather than increasing, their energy (Table 1). In addition, they are slightly less penetrated than in the isolated DMACB molecule. However, the O atoms behave differently. They turn out to be more penetrated than in the gas phase, and no final conclusion could thus be reached on the basis of the use of the *differential* criteria only as to whether the intramolecular H-bonds are becoming weaker or stronger upon formation of the intermolecular ones. More details and a throughout discussion of this delicate point can be found in Ref. [14], while the problem of CH$\cdots$O bonds energetics is addressed below.

3.1.3 *CH$\cdots$O bond energies from the CH$\cdots$O BCP properties?*

The characterization of the energetic features of intermolecular interactions in terms of their BCPs topological properties in crystals has been pioneered by Espinosa et al. [88–90], who proposed the following expressions,[7]

$$D_e = 25.3(6) \times 10^3 \exp[-3.6 \times d_{H\cdots O}] \quad (5)$$

$$- \; D_e \equiv E_{HB} = 0.5 V_b \quad (6)$$

Equations 5 and 6 relate the HB dissociation energy D_e (or the HB energy E_{HB}) with, respectively, the $d_{H\cdots O}$ distance and V_b (Eq. 6), the virial density at the HB CP. The two equations are based on a study of 83 experimentally observed BCPs for X–H$\cdots$O (X=O,N,C) interactions in crystals and on the ab initio evaluation of D_e in a series of gas phase HB systems spanning the same range of

[7] In Eqs. 5–7, energies are in kJ/mol, energy densities in kJ/mol per atomic unit volume and $d_{H\cdots O}$ in Å .

Table 1 DMACB crystal: intermolecular and intramolecular short CH···O interactions [14]. Penetration ΔR of H and O atoms and Δ changes (crystal–molecule) in the H atomic properties upon crystallization

$d_{H\cdots O}$ (Å)	ΔR(H)	ΔR(O)	ΔN(H)	ΔE(H)	ΔV_1(H)
Intermolecular CH···O interactions					
2.351	−0.388	−0.195	−0.067	+0.0271	−4.1
2.453	−0.328	−0.159	−0.048	+0.0182	−4.2
2.517	−0.181	−0.079	−0.037	+0.0137	−2.0
Intramolecular CH···O interactions					
2.211	+0.006	−0.005	+0.036	−0.0200	+0.4
2.219	+0.004	−0.004	+0.036	−0.0185	+2.3
2.232	+0.004	−0.004	+0.033	−0.0195	+1.7

All quantities in au; only the data for the three shorter intramolecular and the three shorter intermolecular (intercolumn) CH···O interactions are reported. ΔN(H), ΔE(H), and ΔV_1(H) represent changes in atomic electron population, atomic energy and atomic volume, respectively. $V_1(H)$ is defined as the portion of the H atomic volume, V(H), where $\rho(\mathbf{r})$ is larger than 0.001 au

$d_{H\cdots O}$ distances of the experimental data set. Equation 6 was obtained by combining Eq. 5 with the following equation:

$$V_b = -50(1.1) \times 10^3 \exp[-3.6 \times d_{H\cdots O}] \quad (7)$$

which reveals an exponential fall-off of $|V_b|$ with the $d_{H\cdots O}$ distance, analogously to what found for G_b [88].

Expressions given in Eqs. 6 and 7 are interesting and of practical use since they relate energetic features at the BCP (V_b, G_b) to the $d_{H\cdots O}$ distance, regardless of the nature of the H-atom acceptor. Furthermore, they also allow for an estimate of the HB energy using only a topological index (V_b), at a single point. However, the inherent limits of validity of these expressions had to be verified [1] since it is well known that the independent atom model (IAM) [5] density and, a fortiori, the sum of non-interacting molecular densities are generally hardly distinguishable from the true density in the intermolecular regions, despite the two model densities are both not containing any information on the intermolecular interactions [14]. Not surprisingly, Spackman [91] could reproduce the exponential dependence of V_b, G_b *versus* the $d_{H\cdots O}$ distance using a simplified two-atoms promolecular model given by the sum of the spherical densities of the H and O atoms. At large separations ($d_{H\cdots O}$ >2.2 Å), where *inter alias* the ρ_b values are close to the unavoidable uncertainty in the experimental electron densities, both V_b and G_b values could hardly be distinguished from the corresponding values of the two-atom promolecular model. This result made us somewhat doubtful about the relevance of V_b and G_b as bonding indices at large $d_{H\cdots O}$ separations as well as about the reliability of the $E_{|HB}$ values obtained from Eq. 6 [1,91].

The case of CH···O interactions in DMACB was even more delicate, since these bonds span a range of distances (2.211 Å < $d_{H\cdots O}$ < 2.969 Å), which extends at larger separations and it is broader than that of Ref. [88] data set (CH···O bonds: 2.22 Å < $d_{H\cdots O}$ < 2.59 Å). Indeed, estimates obtained through Eq. 6 are about twice as large as the estimates given by Eq. 5 for the CH···O DMACB interactions falling in the range of distances considered by Espinosa et al. and even more so for the longer H···O distances. A careful analysis of why the estimates given by the two equations were that different led us to conclude that E_{HB} significantly deviates from $0.5V_b$ in the range of the large H···O distances (2.2 Å < $d_{H\cdots O}$<3.0 Å) and that the estimate given in terms of the $d_{H\cdots O}$ distance (Eq. 7) appears as more reasonable. New equations, fitted on CH···O bonds only, have been proposed by us and the reader is referred to Ref. [14] for a detailed discussion. We concluded that these relationships, as well as those due to Espinosa in their proper range of $d_{H\cdots O}$ distances, rather than as a tool to afford precise E_{HB} estimates, may possibly serve as a simple way to order on a relative energy scale the HBs present in a crystal [14]. We also found that the intramolecular CH···O bond energies in DMACB appear hardly affected by crystallization, in agreement with the contrasting atomic penetration changes discussed earlier for the H and O atoms.

A quantitative analysis of how much the crystal density differs from the total IAM density—not the simplified Spackman's "two-atom" model—was also performed [14]. The IAM density misses two out of the 23 unique intermolecular CH···O BCPs. However, the remaining 21 CH···O contacts, identified by a CP in both densities, turned out to have very similar V_b and G_b values. So, we wondered whether other regions of the crystal space and/or other topological indices bear a more distinctive sign of the onset of these weak intermolecular interactions in the crystal. Indeed, Fig. 3 shows

that the *deformation* and even the *interaction* densities[8] have their minima at the intermolecular BCPs and in the nearby regions, while these densities have much larger magnitudes (well) inside the basins of the interacting H and O atoms. We thought this behavior was quite obvious for the deformation density because this density includes the electron density change due to molecular formation. However, it was for us a bit surprising that a similar picture had emerged also for the case of the interaction density. Rather than in the local properties at its BCP, the sign of a weak intermolecular interaction appears to be definitely more noticeable in the density rearrangements it provokes inside the basins of the interacting atoms. This clearly supports the efficacy of Koch's and Popelier's criteria to establish HBs, and especially so when the HBs which tie together a molecular crystal are very weak. We show below how relevant are the discussed density rearrangements for the molecular dipole value in the crystal.

3.1.4 Role of CH···O interactions: the strong molecular dipole enhancement in the bulk

Table 2 shows that, on passing from the OG molecule in the gas phase to the molecule in the crystal, the RHF theory calculates a dipole moment enhancement of 2.19 au [15]. The induced dipole is about 77% of the gas phase value. Comparison of the crystal geometry (CG) and OG molecular dipoles indicates that the geometry change in the solid accounts for about 20% of the total induced dipole moment, the remaining 80% being due to the matrix effect.[9]

Atomic polarizations give reason for only 2% of this quantity, whereas the dominant contribution comes from the changes in the interatomic charge transfers. A detailed analysis and modeling of such transfers is reported in Ref [15]. It was found that the formation of several CH···O bonds causes an extra small (about 0.2*e*) net flux of electronic charge from the hydrogen atoms of the methyl groups to the carbonyl oxygen atoms, the other atoms in the molecule being much less affected. Despite this small increase of the intramolecular charge transfer, a large $\Delta|\boldsymbol{\mu}|$ arises because the centroids of the positive and negative induced charges lie quite far apart in the molecule, being located on its opposite ends. The fact that changes in the H-atom and O-atom populations upon packing give the dominant contribution to $\Delta|\boldsymbol{\mu}|$ further confirms the importance of such changes in establishing HBs (see earlier). We concluded that the weak CH···O interactions in the DMACB crystal have a very important role since they are able to induce a molecular dipole moment enhancement that is comparable and in most cases even much larger—both in % and absolute value—than that found in systems which are packed together by the much stronger OH···O and NH···O bonds. Ref [15] reports an extensive comparative list for such molecular dipole enhancements.

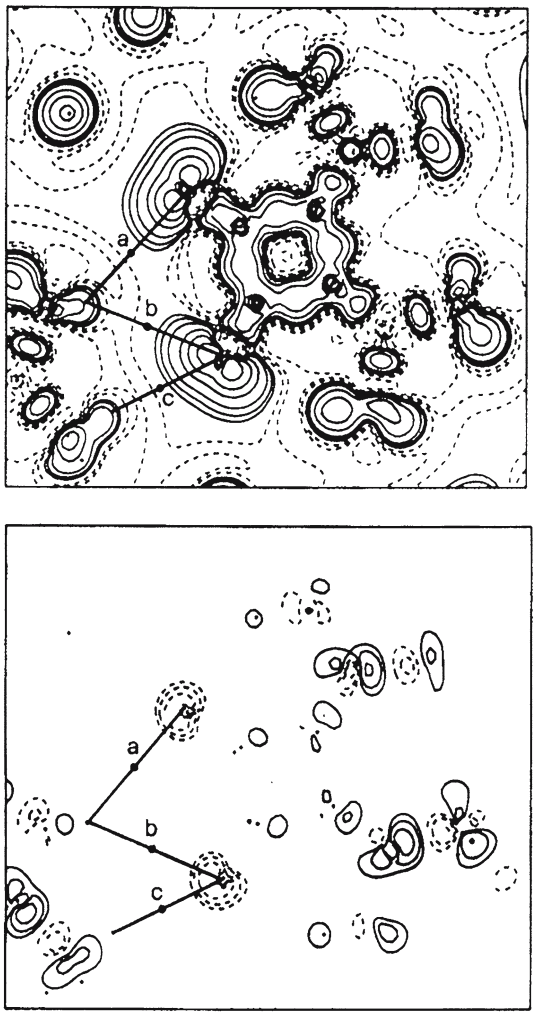

Fig. 3 DMACB crystal. (*Top*) Deformation density (crystal−IAM) and (*Bottom*) Interaction density (crystal−superposition of non-interacting molecules), RHF/6-21G contour plots. Contour levels are at ±2, 4, and 8×10^{-n} au with n ranging from 0 up to 3. *Dotted lines* negative contour levels. Bond paths from three H-atoms to two keto-oxygen acceptors and the associated BCPs are shown (**a** $d_{H\cdots O}$ = 2.453 Å ; **b** $d_{H\cdots O}$ = 2.907 Å ; **c** $d_{H\cdots O}$ =2.942 Å). Information on the intermolecular interactions is at a minimum at and nearby the intermolecular BCPs. The most important changes occur well inside the interacting H and O atomic basins (Reprinted from Fig. 8 with permission from Ref. [14], Copyright 2002 American Chemical Society)

[8] The deformation density is given by the crystal density minus the IAM density (the sum of atomic densities with atoms being placed at the same positions as in the crystal), whereas the interaction density is given by the crystal density minus the superposition of the density of isolated molecules, placed as in the crystal.

[9] The polarization induced by the closest A' neighbor on a A molecule represents only 32% of the matrix effect [15].

Table 2 DMACB crystal: changes of the molecular dipole moment and of its atomic and charge transfer components upon crystallization [15]

Contribution	OG molecule	CG molecule	Crystal
$\boldsymbol{\mu}_{\mathrm{A}}^{\mathrm{a}}$	−1.04	−0.84	−0.86
$\boldsymbol{\mu}_{\mathrm{CT}}^{\mathrm{a}}$	3.89	4.13	5.90
$\lvert\boldsymbol{\mu}\rvert$	2.85	3.29	5.04

RHF/6-21G molecular and periodic wave function data. OG and CG refer to gas phase optimized geometry (C_2) and crystal geometry *A* and *B* isolated molecules. Data for the CG molecule refer to the average of the *A* and *B* molecular dipole; data for the crystal refer to an average over an *A* and a *B* molecule within the crystal. All quantities in au

[a] The components parallel to μ are reported. The projected values amount to 99.9% of the corresponding dipole magnitudes

3.2 Reconstructed clean and chemisorbed silicon surfaces

As we mentioned in Sect. 1, about 10 years ago C.B. Duke proposed that the semiconductor surfaces should be regarded as *truly new bidimensional compounds*, and not merely as a perturbed three-dimensional crystal [22]. Duke's point of view has been pushed a step further in recent years, as an increasing number of chemists have become involved in the functionalization of covalent semiconductor surfaces with organic molecules. In a review on this subject by M.A. Filler et al. [92] surfaces are referred to as *chemical reagents*, whose peculiar reactivity has not much in common with the underlying bulk. Not only the chemistry of semiconductor surfaces differs from the bulk, but also, for a given semiconductor, it strongly depends on the direction of the cut, on the reconstruction pattern, and on the chemical species—if any—bound to the surface atoms. The subtle interplay between surface atoms, attached chemical species, and the underlying bulk, has no counterpart in molecular chemistry nor in solid-state physics, and it is disclosing new territories in the area of nanotechnologies.

The atomic and geometric structure of surfaces are quite accessible experimentally: the reconstruction pattern, the displacements of the surface atoms from the ideal bulk-like positions, and the exact location of adsorbed species can be determined with a high degree of accuracy using many techniques, such as low energy electron diffraction (LEED) [93] scanning tunnelling microscopy (STM) [94] and X-rays or electron diffraction [23]. A wide range of spectroscopical techniques can provide information on the electronic structure, i.e., on the energy distribution of the surface electronic states, but little is known about the EDD $\rho(r)$ of surfaces. Some features of ρ(r) can be recovered by STM, but this method is essentially limited to the regions far from the nuclei, where the electron density is decaying towards the vacuum. The recent improvements in electrons and X-ray diffraction techniques are very promising; however, if recovering directly the three-dimensional EDD of a regular surface is in principle possible, the necessary degree of precision in the collected data is still far from being reached. To the best of our knowledge, there is a single such application, a study on Si(001)(2×1)-H, where $\rho(r)$ could be recovered only by combining experimental data and electron densities coming from ab initio computations [95].

With the aim of stimulating and challenging future experiments in this field, we carried out theoretical electron density studies on a number of clean and hydrogen covered silicon surfaces (Fig. 4). Systems were selected among the ones mostly used by the experimentalists. The geometrical features of all these surfaces but one are well known, as well as the perturbation induced by the surface states on the electronic band structure, while very little or no information on their EDD was available before our first studies on these systems had appeared [24,25].

3.2.1 Systems studied

We considered six silicon surfaces, whose stick-and-ball representations are reported in Fig. 4: Si(111)(1×1), Si(111)(2×1), Si(111)(1×1)–H, Si(100)(2×1), Si(100)(2×1)–H and Si(100)(1×1)–2H.

Si(111)(1×1) is just the truncation of the bulk network along the (111) plane. It is not stable experimentally, and reverts to more complex reconstruction patterns. We studied it for its simplicity, and as a reference ideal system with no geometrical reconstruction, and where each surface atom presents an unpaired electron. One of the reconstruction patterns for the clean Si(111) system is the (2×1). Its structure has been determined experimentally either with quantitative LEED [96–98] and medium energy ion scattering (MEIS) [99] experiments, and involves large displacements of the first two silicon layers through the formation of infinite chains of surface atoms which are threefold coordinated and in a nearly planar arrangement. In analogy with the molecular chemistry of carbon, in Si(111)(2×1) the dangling bonds should be saturated by formation of double

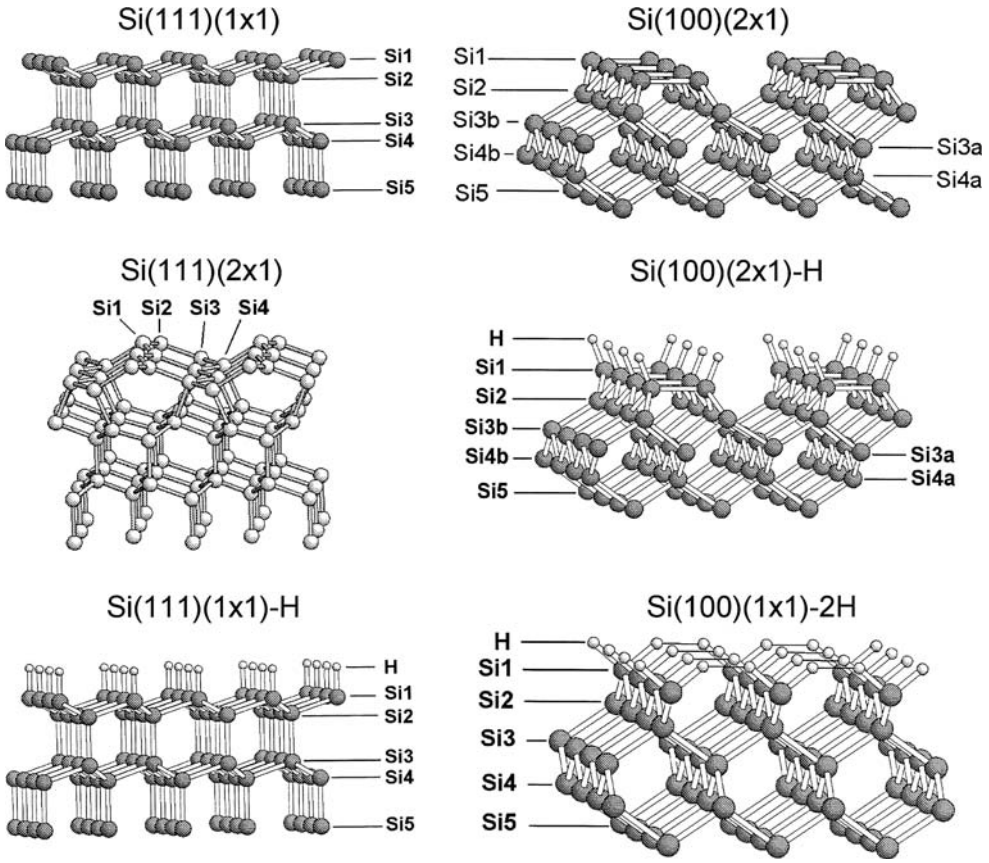

Fig. 4 Stick and ball representation of the surfaces considered in our investigation. Only half of the centrosymmetric slabs adopted to model these surfaces is shown

bonds along the infinite Si1–Si2 chains (see Fig. 4), and this observation is supported by angle resolved photoemission spectroscopy experiments [100–102], which detected a dispersion in reciprocal space of the surface electronic states compatible with π bonding. This is a strong point of interest, because at present we know no stable molecule with Si–Si double bonding, despite this reconstructed surface has been interpreted by Pandey in terms of a π-bonded chain model [103]. Whatever the reconstruction pattern of Si(111), its hydrogenation affords Si(111)(1×1)–H, which is the simplest H-covered silicon surface. Its structure reproduces the truncated bulk network but for a small relaxation and minor changes of the distances between the outermost silicon layers. The Si(111)(1×1)–H surface has been the subject of several experimental [104–106] and theoretical [107–110] investigations.

The clean Si(100)(1×1) surface is another unstable system and reconstructs. The atoms of the outermost layer undergo large displacements to form dimers (Fig. 4), and induce significant strain in the underlying bulk-like network. The simplest pattern corresponds to (2×1) surface cells containing one symmetric dimer each, as shown in Fig. 4. There are also more complex proposals, which explore the possibility that dimers are non-symmetric, and arrange in extended ordered domains [111,112]. In the present discussion, we will consider just the (2×1) symmetric dimer model, as it is widely accepted that further distortions induce just small perturbations of the surface electronic structure. Similarly to Si(111)(2×1), also in Si(100)(2×1) the outermost silicon atoms are formally threefold coordinated. Hence, the formation of double bonding within dimers would saturate the dangling bonds on Si1, although there is not much information about this aspect. Hydrogenation of the clean Si(100)(2×1) surface may produce Si(100)(2×1)–H, Si(100)(1×1)–2H, or intermediate species, depending on the experimental conditions. In the first case, the π, bonding within silicon dimers, if present, is removed, and the dimers remain or become symmetrical, as confirmed by an accurate experimental investigation [113]. Further hydrogenation breaks the silicon dimers, and should produce Si(100)(1×1)–2H, where every atom of the outermost layer is bonded to two hydrogen atoms, and the Si–Si bonding network is bulk-like (see Fig. 4). However, no regular extended

domains of Si(100)(1×1)–2H surface has been observed experimentally, and atomic level STM studies always reveal the presence of disordered, distorted mixtures of Si(100)(2×1)–H, Si(100)(1×1)–2H, and more complex structures whose stoichiometry and geometrical arrangement is not easily determined [114]. To explain this phenomenon is another key point of our studies.

3.2.2 Computational details

The wave functions for the surfaces have been computed with the CRYSTAL code, using a slab model to account properly for their 2D periodicity. We considered slabs consisting of ten silicon layers, so that the electronic structure of the two innermost silicon layers is converged to the bulk material [25]. For all surfaces, we optimized the relevant geometrical parameters, to study the relaxation and reconstruction effects, with the exception of Si(111)(2×1). In this system, there are relevant atomic displacements up to the sixth layer, and a full optimization procedure was too computationally demanding. We therefore adopted two experimental geometries, coming from different experiments [97,99] and a slab consisting of 14 layers, to ensure that the innermost atoms are bulk like, at least as for the geometrical arrangement.

The systems wave functions have been computed using different Hamiltonians, and Gaussian basis sets specifically optimized [24,25] for silicon; some details are reported in Table 3. For the sake of simplicity, we will describe just Hartree–Fock results obtained with the 3–21G(d,p) basis set, which always proved to reproduce correctly the electronic properties of these systems. For the H-covered surfaces, and for the clean Si(111)(1×1), we adopted a Restricted Hartree–Fock scheme, while the Unrestricted approach proved more appropriate for the other clean surfaces [24]. In these systems, we also tested different spin alignments of the outermost surface atoms, to control the formation and the breaking of the π-bonded structure.

3.2.3 Truncation of bulk silicon along the (111) plane, reconstruction and passivation

In this section we summarize the main results of our investigation of Si(111) surfaces, which are extensively discussed in Refs. [24,25]. Crystalline silicon has a diamond-like crystal structure and, as anticipated from this structure, the QTAIM analysis of the crystal electron density finds each atom to be bonded to the four equivalent first neighbors, located at 2.37 Å . The topological bonding properties are consistent with the covalent nature of this interaction, and are reported in Table 4. The EDD at the BCP has cylindrical symmetry, as expected for the pure σ bonds of bulk silicon.

The negative of the Laplacian of $\rho(r)$, $\mathbf{L}(r) = -\nabla^2\rho(r)$, has four maximums in the valence region of each silicon, pointing towards the bonded neighbors. In the following these maximums will be referred to as *bonded charge concentrations* (BCC), as opposed to the maximums of L(r) not directed towards bonded neighbors (a case not occurring in bulk silicon) that will be referred to as *non bonded charge concentrations* (NBCC).

Consistently with the crystal symmetry, silicon atoms have zero net electrostatic charge q(Ω), and no atomic dipole $\boldsymbol{\mu}(\Omega)$. Every crystallographic cell contains 8 silicon atoms, and hence the volume V(Ω) of each atom's basin is exactly 1/8 of the cell. In surfaces V(Ω) may extend infinitely towards the vacuum, and therefore we considered V1(Ω), the portion of V(Ω) where $\rho(r)$ is larger than 0.001au. In the bulk material there is no relevant difference between V and V1 since there are no low electron density regions.

The truncation of the bulk along the (111) plane generates a layer of silicon atoms with just three neighbors at 2.37 Å, as can be seen from Fig. 4. This is a radical perturbation, but induces only minor changes on the bonding properties, as evinced from Table 4 and Fig. 5. Every Si1 atom is left three bonds with Si2 ones, but they are just slightly weakened as compared to bulk: the BCP remains close to the internuclear midpoint and the corresponding ρ_b and L_b values reduce by few percent. The other bonds are even less perturbed.

There is one valence electron on each Si1 atom which is not involved in bonding, but it is not transferred to the inner layers, since all the atoms remain nearly neutral (see Table 5). Nevertheless, the surface/vacuum interface induces a large rearrangement of the EDD within the atomic basin of Si1: the atomic volume V1 is increased by about 20% as compared to the bulk; the atomic dipole is quite large, 0.23 au, and points inwards. These effects indicate that the $\rho(r)$ of Si1 expands towards the vacuum and becomes more diffuse as compared to the bulk atoms.

In the wave function determination, we forced the formation of dangling bonds on Si1 by locking the spin alignment; and their presence is efficiently revealed by the topology of the Laplacian (see Fig. 5). The Si1 atom has three BCC directed along Si1–Si2, and their properties are essentially bulk-like (Table 6); a fourth maximum points towards the vacuum, and is much less sharp than the BCC: $\rho(r)$ and L(r) at the NBCC are lower by 34 and 60%, respectively, as compared to the bulk BCC.

The bonding and atomic properties of the inner layers converge very rapidly to the bulk. In conclusion, the electron density of Si(111)(1×1) is perturbed essentially

Table 3 Silicon surfaces: details of the Hamiltonians and basis sets adopted

Surface	Hamiltonians [a]	Basis sets [b]
Si(111)(1×1)	ROHF	3-21G, 3-21G(d)
Si(111)(1×1)–H	RHF	3-21G, 3-21G(d,p)
Si(111)(2×1)	RHF, ROHF, UHF($\alpha\beta$), UHF($\alpha\alpha$), LDA, B3LYP($\alpha\beta$), B3LYP($\alpha\alpha$), PWGGA($\alpha\beta$)	3-21G(d)
Si(100)(2×1)	UHF($\alpha\beta$), UHF($\alpha\alpha$), B3LYP($\alpha\beta$), B3LYP($\alpha\alpha$)	3-21G(d)
Si(100)(2×1)–H	RHF, B3LYP	3-21G(d,p)
Si(100)(1×1)–2H	RHF, B3LYP	3-21G(d,p)

[a] In the case of unrestricted spin schemes, we report the starting electron spin alignment—($\alpha\beta$) or ($\alpha\alpha$)—of neighboring silicon atoms belonging to the outermost layer
[b] The contraction factors of the two outermost *sp* shells of the basis sets were optimized along with the cell parameter of bulk silicon, as described in Refs. [24,25]

Table 4 Bonding properties in clean and H-covered surfaces according to the QTAIM formalism

System	Bond	R [a]	Δ_{BCP} [b]	$\rho_b \times 10^2$ [c]	$L_b \times 10^2$ [c]	$(\lambda_3 \times 10^2)_b$ [c]	ε_b [c]
Bulk	Si–Si	2.37	0.0	8.49	11.6	2.6	0.00
Si(111)(1×1)	Si1–Si2	2.37	0.0	8.40	11.1	2.7	0.04
Si(111)(2×1)	Si1–Si2	2.27	+0.1	8.99	12.5	1.7	0.26
	Si1–Si4	2.38	0.0	8.10	10.3	2.8	0.08
	Si2–Si3	2.31	0.0	8.67	11.9	2.4	0.12
Si(100)(2×1)$\alpha\alpha$	Si1–Si1	2.45	0.0	6.98	6.7	3.8	0.06
	Si1–Si2	2.37	+0.7	8.02	9.7	3.3	0.05
Si(100)(2×1)$\alpha\beta$	Si1–Si1	2.41	0.0	7.41	7.6	3.6	0.10
	Si1–Si2	2.37	+0.1	8.07	9.9	3.2	0.07
Si(111)(1×1)–H	Si1–H	1.49	+4.1	11.40	−38.2	76.6	0.00
	Si1–Si2	2.36	−1.4	8.83	13.3	2.1	0.02
	Si2–Si3	2.38	+0.8	8.53	12.1	2.2	0.00
Si(100)(2×1)–H	Si1–H	1.49		11.47	−34.7	74.0	0.00
	Si1–Si1	2.42	0.0	8.26	11.2	3.0	0.06
	Si1–Si2	2.37	−0.9	8.57	11.9	2.7	0.01
Si(100)(1×1)–2H	H–H	1.65	0.0	2.73	−7.3	14.5	0.05
	Si1–H	1.45	+2.8	12.56	−44.1	89.1	0.01
	Si1–Si2	2.35	−0.7	8.95	13.4	2.4	0.01
H–H $\alpha\beta$	H–H	1.65	0.0	4.51	2.8	9.3	0.00
H–H $\alpha\alpha$	H–H	1.65	0.0	2.21	−6.7	13.3	0.00

[a] Internuclear distance (Å)
[b] Shift of the BCP with respect to the A–B midpoint: negative values indicate that the BCP is closer to A and vice versa
[c] The "b" subscript denotes values (au) for these quantities at the BCP

only at the surface/vacuum interface, where it becomes more diffuse and polarizes outwards.

The (1×1) to (2×1) reconstruction of Si(111) involves large displacements of the atoms of the first two layers, generating a completely different bonding pattern (see Figs. 4, 5). As for the notation, the Si1 atoms of Si(111)(1×1) split in Si1 and Si2 in Si(111)(2×1), while Si2 split in Si3 and Si4 (see Fig. 4). In this surface, the atoms threefold coordinated, Si1 and Si2, are bonded to each other and form infinite zigzag chains in a nearly planar arrangement, a situation consistent with π-bonding. In fact, the Si1–Si2 bond is markedly stronger than in the bulk: ρ_b and L_b increase by 6 and 8%, respectively, and the positive curvature λ_{3b} drastically decreases by about 40%, denoting an increased accumulation of charge along the BP. Moreover, the ellipticity is large, 0.26, and with the π-plane being normal to the surface cut and containing the Si1–Si2 internuclear axis. The averaged bonding properties of Si1–Si4 and Si2–Si3 indicate a slight weakening as compared to the bulk, as happens for Si1–Si2 in the (1×1) clean surface. The topology of $L(r)$ (Table 6) reveals that only the Si1 atoms present a NBCC, and even less pronounced than in Si(111)(1×1), while the Si2 atoms have just three BCC. We can affirm that the strain induced in the lattice by the formation of Si1–Si2 chains is balanced by the formation of an incomplete, delocalized π-bonding structure, which saturates half of the dangling bonds, and depletes the NBCC of the remaining ones.

As for the atomic properties, the outermost layer remains almost neutral, as $[q(\text{Si1})+q(\text{Si2})]/2$ equals $-0.04e$, and the atomic volumes of Si1 and Si2 increase

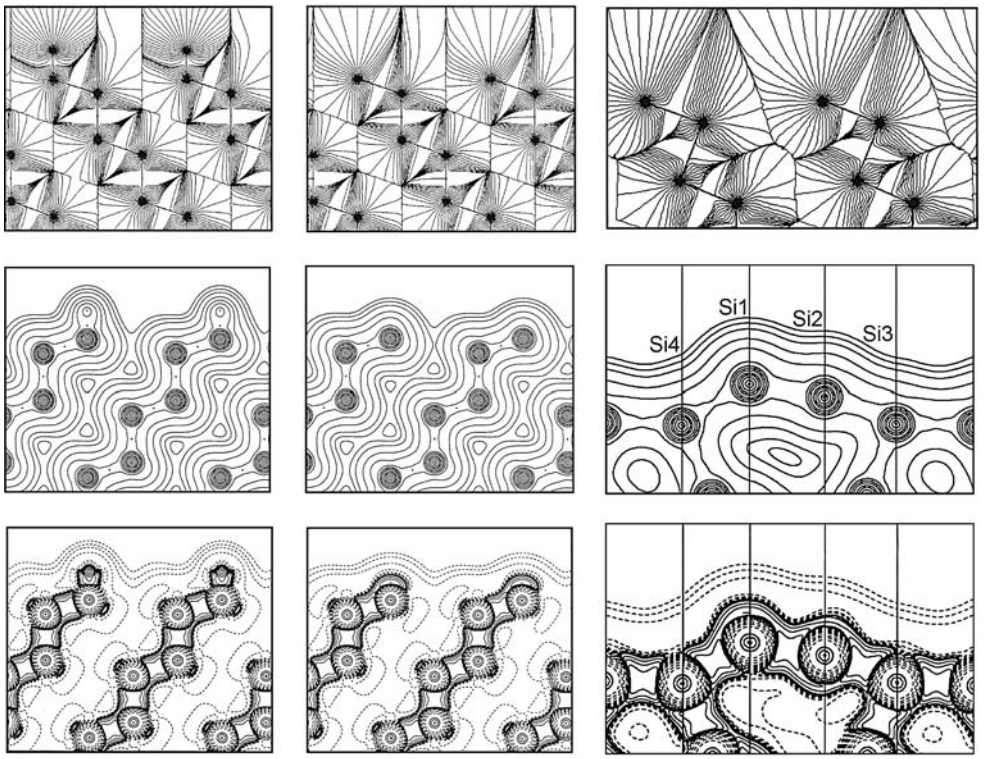

Fig. 5 From left to right: Si(111)(1×1)–H, Si(111)(1×1), and Si(111)(2×1) surfaces; from *top to bottom*: gradient paths of the electron density, contour levels of the electron density, contour levels of the Laplacian of the electron density (*full/dashed lines* represent negative/positive values). Plots for the (1×1) surfaces refer to planes normal to the slabs' surfaces and containing Si1 through Si5 nuclei. In the case of the (2×1) surface: (*top*) $\nabla\rho$ trajectories and bonding pattern in a plane normal to the surface of the slab and containing Si2–Si3 bonds; (*middle and bottom*) contour plots in five different planes normal to the surface and juxtaposed so as to show the whole bonding network among the atoms of the two outermost layers. Adjusted from Fig. 3 with permission from Ref. [25], and from Figs. 3 and 4 with permission from Ref. [24]

Table 5 Atomic properties in clean and H-covered surfaces

System	Ω	q(Ω) [a]	Δ V1(Ω) [b]	$\lvert\boldsymbol{\mu}(\Omega)\rvert$ [c]	$\mu_z(\Omega)$ [d]
Si(111)(1×1)	Si1	−0.02	+25.1	0.23	−0.23
	Si2	+0.02	+2.5	0.06	+0.06
Si(111)(2×1)	Si1	+0.14	+28.2	0.50	−0.39
	Si2	−0.22	+35.3	0.17	+0.08
	Si3	+0.01	+4.8	0.21	−0.12
	Si4	+0.07	+0.5	0.11	+0.07
Si(100)(2×1) $\alpha\alpha$	Si1	+0.04	+48.6	0.30	−0.29
	Si2	−0.07	+7.4	0.11	−0.04
Si(100)(2×1) $\alpha\beta$	Si1	0.00	+47.7	0.34	−0.31
	Si2	−0.03	+6.0	0.12	+0.07
Si(111)(1×1)–H	H	−0.74		0.43	
	Si1	+0.70	−18.1	1.23	1.23
	Si2	+0.05	+0.1	0.03	−0.03
Si(100)(2×1)–H	H	−0.73		0.42	
	Si1	+0.74	−19.7	1.19	
	Si2	0.00	+5.2	0.18	−0.04
Si(100)(1×1)–2H	H	−0.74		0.49	
	Si1	+1.51	−48.5	1.50	+1.50
	Si2	−0.01	+3.4	0.03	−0.03

[a] Net atomic charge, au
[b] Deviation of the atomic volume V1 with respect to the bulk value of 138.7 au
[c] Norm of the atomic dipole (au)
[d] Component (au) of the atomic dipole normal to the surface cut. Positive and negative values indicate that the dipole component points outwards and inwards, respectively

Table 6 Properties of some charge concentrations (CC) in clean and H-covered surfaces according to the QTAIM formalism

System	Ω [a]	Neighbor [b]	d [c]	$\rho_{cc} \times 10^{2}$ [d]	$L_{cc} \times 10^{2}$ [d]
Bulk	Si	Si	0.90	8.74	16.4
Si(111)(1×1)	Si1	Vacuum	0.90	5.74	9.8
	Si1	Si2	0.91	8.66	15.7
Si(111)(2×1)	Si1	Vacuum		5.45	8.2
Si(100)(2×1) $\alpha\alpha$	Si1	Vacuum	0.90	5.47	8.1
	Si1	Si1	0.90	7.53	11.8
	Si1	Si2	0.90	8.37	14.4
Si(100)(2×1) $\alpha\beta$	Si1	Vacuum	0.90	5.34	7.7
	Si1	Si1	0.90	7.86	12.6
	Si1	Si2	0.90	8.52	14.4
Si(111)(1×1)–H	Si1	Si2	0.90	9.02	18.1
Si(100)(2×1)–H	Si1	Si1	0.90	8.59	16.8
	Si1	Si2	0.90	8.84	17.3
Si(100)(1×1)–2H	Si1	Si2	0.90	9.15	18.8

[a] Atom whose valence shell contains the CC
[b] Neighbor directed along Ω . . .CC
[c] Ω . . .CC distance Å
[d] electron density at the CC and negative of the Laplacian of the electron density at the CC, both in au

by 32 au on average. However, the atoms pushed outwards the surface, Si1, highly differ from the Si2 ones, which—as mentioned earlier—play the major role in the formation of π-bonding. Si1 atoms are positively charged (+0.14*e*), and their electron density is transferred towards Si2 atoms (−0.22*e*). The electron density of Si1 atoms is polarized towards the vacuum (negative $\boldsymbol{\mu}_z$ value, Table 5) as happens for the Si1 atoms in Si(111)(1×1), while no such effect is found for the Si2 ones.

In conclusion, double bonding is indeed the driving force of the (1×1) to (2×1) reconstruction of Si(111), a situation with no analogy in molecular chemistry. It causes half of the surface atoms, the Si2 ones, to become markedly different from the silicon atoms in both the Si(111)(1×1) and the Si bulk reference systems. Interestingly, also the bonds between the first and the second layer (Si2–Si3, Si1–Si4) as well as those within the second layer (Si3–Si4) possess significant ellipticities [24]. It is clearly an indication that the π-conjugation extends over a 2D array of bonds and not just along the topmost layer 1D chains, as hypothesized by the Pandey's model [103].

After hydrogen passivation, Si(111) forms a bulk-like bonding network, as shown in Fig. 4. The Si1 atoms are bonded to three Si2 and one H atom, in a nearly tetrahedral arrangement. The atomic basin of Si1 is largely shrunk, and the Si1 atoms are now isolated from any interaction with the outside, as shown in Fig. 5, while Si2 are not. The H atoms bear a large and negative electronic charge, about −0.75*e*, and such charge transfer from silicon is compensated for almost entirely by the atoms of the outermost layer.

The atomic dipoles of the atoms forming Si–H bonds are much larger than found in clean surfaces, and point both upwards, which means that the electron density of H preferentially accumulates towards Si1, and the one of Si1 towards Si2. Si1 and H atoms polarize in such a way as to oppose the electric field generated by the charge transfer from Si to the H, as it happens in diatomic hydrides [6].

The reversal of the polarization of Si1 upon hydrogen coverage induces a noticeable strengthening of the bonds with Si2 atoms. Comparing the clean to the H-covered Si(111) surface the ρ_b and L_b values increase by about 5 and 20%, respectively, and Si1–Si2 becomes even stronger than in the bulk.

The topology of $L(r)$ (Table 6) shows that the NBCC of Si1 present in clean surfaces disappears upon hydrogen coverage, and the Si1 atoms has no BCC pointing towards H. The dangling bonds of the clean Si(111) are not just saturated, but the electron density at the surface/vacuum interface is transferred to the H. Consistently with the atomic polarization induced by hydrogenation, the BCC of Si1 associated to Si1–Si2 bonds becomes more pronounced.

The electronic structure of the inner silicon layers is not significantly perturbed: starting from the third layer inwards Si(111)(1×1)–H assumes the properties of the bulk material.

3.2.4 Truncation along (100) and reconstruction: clean and H covered Si(100)(2×1) surfaces

In the present and the next sections, we will discuss the properties of the Si(100) surfaces, stressing their

analogies with those discussed earlier for the cut, reconstruction and passivation of bulk silicon along the (111) plane. The results presented here have never been published before.

Truncation along the (100) plane leaves each surface atom with two dangling bonds. The (2×1) reconstruction involves the formation of dimers, as shown in Fig. 4: the threefold coordinated atoms of the outermost layer are bonded to each other, similarly to Si(111)(2×1). In the clean surface this arrangement is consistent with π-bonding, which contrary to Si(111)(2×1), should be localized on Si1–Si1 dimers, and not delocalized along infinite chains. Since the double bonding within dimers in Si(100) is not well established, we considered two different spin alignments for each Si1–Si1 pair: the singlet $\alpha\beta$, where double bonding is allowed, and the triplet $\alpha\alpha$, where pairing between π-electrons is precluded, thus ensuring a Si1–Si1 pure σ-bond.

The Si1–Si1 internuclear distance is larger than in the bulk, regardless of the spin alignment, and moving from the triplet to the singlet it shortens by 0.04 Å . Bond and electronic properties, as discussed below, reflect these peculiar structural results.

Despite a different cut plane and a different bonding network, the clean Si(100)(2×1) surface resembles more closely the unreconstructed Si(111)(1x1) surface than the Si(111)(2×1) reconstruction, as clearly shown by the analysis of data in Tables 4, 5 and 6. The Si1 atoms remain nearly neutral; their atomic volume exceeds the bulk value by about 50 au and the atomic dipole is large and points downwards. The electron density in fact polarizes towards the vacuum and becomes more diffuse, as observed for Si1 in Si(111)(1×1). Consistently, the bonds between the first and the second silicon layers are slightly weakened as compared to the bulk. The Laplacian of Si1 atoms exhibits a maximum directed towards the vacuum and three BCC; the NBCC of the singlet and the triplet wave functions are very similar to each other, and slightly less peaked as compared to the NBCC in Si(111)(1×1). The Si1–Si1 σ-bond of the triplet wave function appears significantly weaker as compared to the bulk case: ρ_b is lower by 18%, and L_b by 42%; the electron density at BCP shows small accumulation in the direction normal to the surface, namely the π-plane. In the singlet wave function, the Si1–Si1 bond strengthens, but remains still weaker than a bulk σ-bond, and there is no evidence for a significant increase in accumulation of electron density in the π-plane. In conclusion, the spin alignment does not play a major role in Si(100)(2×1): the pairing between the two dangling bonds in the π-plane of dimers is very weak, as happens for the molecular chemistry of silicon, and contrary to what observed for Si(111)(2×1). Therefore, the driving force of the (2×1) reconstruction is the formation of a Si1-Si1 σ-bond, which is weaker than the σ-bond in the bulk and which saturates one dangling bond out of the two for every Si1 atom.

Also the Si(100)(2×1)–H surface is very similar to the Si(111)(1×1)–H one. Upon H passivation about 0.75*e* are transferred from silicon to H, with Si1 atoms carrying more than 90% of the resulting positive charge on silicon atoms. The dangling bond disappears on Si1, which shows an atomic dipole largely increased and reversed. The polarization of Si1 towards the inside makes its BCC more pronounced, and induces a noticeable strengthening of the bonds with the other silicon atoms. Interestingly, this effect is larger for Si1–Si1 than for the Si1–Si2 bond, regardless of the spin alignment of the reference clean system, a further indication that hydrogenation of Si(100)(2×1) does not involve the rupture of a strong Si1–Si1 double bond.

The peculiar feature of the *symmetric* Si(100)(1×1)−2H surface is that the H atoms bonded to neighboring Si1 atoms are unusually close to each other, about 1.65 Å far apart, and form H–H dihydrogen "bonds" [115] as revealed by the occurrence of a BP linking the two H atoms. This kind of interactions, which is customarily associated by chemists to the presence of non bonded or even "repulsive" H ··· H contacts, is currently being highly debated in the literature [42–44]. The properties and the role such interactions have on the geometrical structural and EDD of Si(100)(1×1)–2H are discussed in the next section.

3.2.5 Steric effects and disorder in Si(100)(1×1)-2H

To form the Si(100)(1×1)–H surface hydrogen should be adsorbed onto the clean Si(100) in a 2:1 ratio with Si1 atoms, a task which has been afforded in several ways by the experimentalists. However, there is no evidence that such process produces the regular *symmetric* surface reported in Fig. 4, where the bonding network is bulk-like except for relaxation of the distance between the silicon layers. Furthermore, STM images suggest that this system invariably contains a disordered mixture of Si–H, Si–H_2 and Si–H_3 species, as well as more complex defects [114]. As will be discussed below, we found strong indications that the *symmetric* Si(100)(1×1)–2H surface might be unstable.

The analysis of the geometrical structure of the *symmetric* surface suggests the presence of strain within the Si1–H_2 groups. First, the Si–H bonds are 0.04 Å shorter than the value of 1.49 Å found in the other surfaces. Second, the H–Si1–H angle measures 100°, significantly smaller than the ideal tetrahedral value of 109°. Clearly, a longer Si–H distance and a larger H–Si1–H

angle would shorten the internuclear distance of 1.65 Å between H atoms bonded to neighboring Si1 atoms.

As for the EDD, each H atom form two bonds (see Fig. 6), one with Si1 and the other with another H, which is quite unusual for this element. The data in Table 4 clearly shows that H–H are closed shell interactions, because the value of $L(r)$ at the BCP is large and negative, and λ_3 is large. More importantly, these bonds are very similar to the highly repulsive spin triplet H–H system at R(H–H) = 1.65 Å, while completely differ from the attractive spin singlet H–H case at the same distance.

The complete optimization of the surface geometry requires to lower its symmetry, and the Si1–H_2 groups significantly bend, but remain in the original plane defined in the *symmetric* surface, as reported in Fig. 6. The distance between Si1 and Si2 does not change noticeably, but Si1 is about 10° out from the ideal tetrahedral arrangement. The Si1–H1 and Si1–H2 distances elongate to 1.48 and 1.47 Å, respectively, and the H1–Si1–H2 angle increases up to 103°. As a consequence of such distortions, the H1–H2 distance reaches 1.90 Å, 0.25 Å larger than in the *symmetric* surface. The H–H bonds are present also in the *non-symmetric* surface, and their properties are still very similar to a spin triplet H–H molecule, but they are much weaker: ρ_b and L_b decrease by 25 and 16%, respectively, as compared to the *symmetric* surface.

The above discussion calls for some remarks. First, we agree that no regular domain of the *symmetric* Si(111)(1×1)–2H should be found experimentally: it is not the absolute energy minimum for this surface, and we found no relevant energy barrier during the conversion into the *non-symmetric* ground state. Second, even the formation of regular *non-symmetric* domains remains to be demonstrated: the Si2–Si1–H_2 bonding network appears quite distorted, and the presence of defects at the surface would probably help in releasing such a strain. The rearrangement of the Si1–H_2 groups around point or extended defects might prevent the formation of regularly ordered extended domains, where all Si1–H_2 groups arrange with the same orientation. Finally, we suggest that the STM signals coming from Si(100)(1×1)–H might be not correctly interpreted, even with respect to the surface stoichiometry. As can be seen from Fig. 6, the contribution to the electron density above the surface, which roughly corresponds to the signals collected by STM, comes almost entirely from H1 atoms, whose atomic basins completely fill the surface/vacuum interface. The H2 atoms are much closer to the silicon layers, and their atomic basins noticeably more compressed, and hence they might not be detected at the usual STM surface scanning conditions. Moreover, possible changes in the orientation of the Si1H_2 groups close to surface defects might further on complicate the picture obtained by STM.

4 Applications to materials science

Our involvement and role in two cooperative material science projects has been summarized in Sect. 1. Here we briefly review our work on bond and point defects in silicon and we then illustrate in some more detail our very recent, and partly yet unpublished work on TE materials.

4.1 Bond and point defects in Si

The migration and interaction of native point defects in silicon is known to influence important properties of the bulk samples such as the mass transport, the annealing of implantation damage, the crystal-to-amorphous transition and the nucleation of extended defects. If the coalescence of *like* defects in silicon determines intermediate steps for the formation of microdefects, like voids or dislocation loops, the interaction between defects made of *different* species governs the microstructural evolution far from equilibrium, e.g., during ion implantation.

The annihilation of a vacancy–interstitial pair is one of these latter interactions. When a single vacancy (V) and a self-interstitial (I) approach each other from distances larger than two bond lengths, a new defect, named *I–V complex* is formed [116]. This is not a number defect, since it does not involve any deficit or excess of atoms. Rather, we called it a BD [27] because in the complex two linked silicon atoms (A and A′, Fig. 7) have one of their neighbors interchanged with respect to the ideal structure. The annihilation path of the *I–V* complex requires a sizeable perturbation in the bond pattern of the host matrix and it could thus play an important role in the microstructural evolution of silicon in various conditions. The aim of our work has been that of providing an accurate atomic-scale description of the BD's electronic structure and bonding pattern and to follow their evolution along the annihilation reaction path which recovers the usual diamond lattice. We used 216-atom TBMD (tight binding molecular dynamics) simulations to generate the defect geometrical structures along the path and performed RHF calculations and QTAIM analysis on sizeable clusters (32 Si and 38 pseudohydrogen atoms) obtained from these structures. Our calculations confirmed that the BD complex rearranges to the non-defective system through a significant energy barrier (about 1.3–2.0 eV, according to the computational level). The QTAIM analysis predicts that all the Si atoms retain a fourfold coordination along the

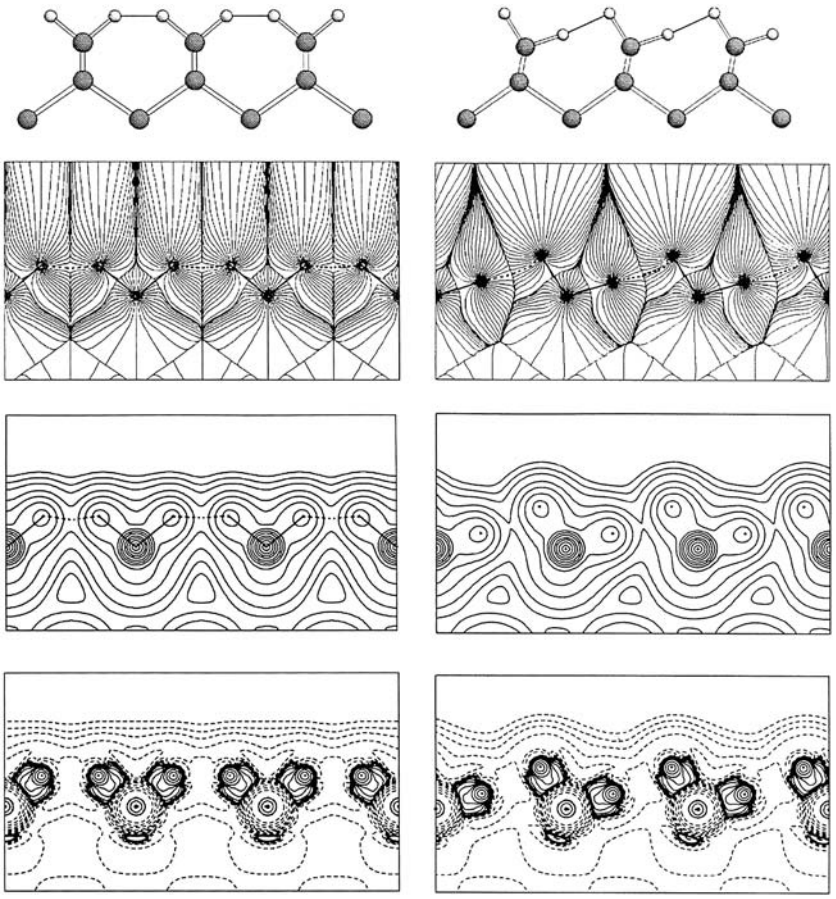

Fig. 6 Si(100)(1×1)–2H surface: *left panels, symmetric* energy minimum; *right panels*: *non-symmetric* energy minimum. From *top to bottom*: stick-and-ball representation of the surface; gradient paths of the electron density, with H–H bond paths superimposed as dashed lines; contour levels of the electron density; contour levels of the Laplacian of the electron density (*full/dashed lines* represent negative/positive values)

path, but the properties of the bonds within the complex change dramatically. Figure 7 shows contour plots of the electron density and of its Laplacian for the BD complex along its annihilation path, with the reaction coordinate s being 0 for the complex and 1 for the non defective system. The BCP properties of the BD complex (Table 7) indicate noticeable changes with respect to the ideal structure, as caused by the marked shortening of the AA′ bond and lengthening of the AB type bonds. However, all bonds remain basically covalent as in the perfect lattice, with low bond ellipticity values and thus nearly pure σ-character. Conversely, at the top of the barrier (s=0.33), the Si–Si bonds have a quite different nature with respect to either those in the BD complex and in the nondefective system. The A (A′) atoms are only formally fourfold coordinated for they exhibit three covalent, nearly coplanar, strong bonds, with large ellipticity values, and a fourth very weak (low ρ_b, positive $\nabla^2\rho_b$) closed-shell bond pointing out of this plane. The hybridization of A(A′) atoms is thus much closer to sp^2 rather than sp^3, a result confirmed by the vanishing of the BCC pointing towards B(B′) atoms and the accompanying increase in the BCCs of the remaining bonds. In the BD complex about 0.5 electrons are withdrawn from the defective atoms (2A+2B+4C set of atoms, Fig. 7) and this charge leakage from the BD complex to the surrounding persists over the BD annihilation path, except, obviously, close to $s = 1$. What changes along s is the relative contribution of the defective atoms: the more unbalanced the charge removal from the defective atoms, the higher is the energy destabilization with respect to the ideal system. This observation, along with the Laplacian analysis discussed above, provides chemical insight as for the existence of a significant barrier for the BD annihilation: a large charge transfer within the defective atoms $[q(B) = 0.294, q(C) = -0.772]$ and a significant re-hybridization is found to characterize the top of the barrier.

A similar computational approach was also adopted in our study [28] of the evolution of energetics and bonding of compact self-interstitial $(SI)_n$ clusters in silicon (n denotes the number of atoms in the cluster). Formation and growth of $(SI)_n$ clusters in crystalline silicon occurs whenever a number of excess Si atoms are created in the host diamond lattice, which are then free to interact—a scenario typical of silicon ion beam processing

Table 7 Si–Si BCP properties along the bond defect (BD) complex annihilation path

Bond	R (Å)	ρ_b	$\nabla^2\rho_b$	ε_b
$s = 0$ (BD complex)				
A–A′	2.27	0.081	−0.104	0.04
A–B	2.46	0.064	−0.056	0.01
A–C	2.39	0.070	−0.072	0.02
$s = 0.33$ (top of the barrier)				
A–A′	2.27	0.084	−0.114	0.12
A–B	3.01	0.030	+0.013	0.41
A–C	2.33	0.074	−0.071	0.12
$s = 1.00$ (non-defective system)				
A–A′	2.36	0.073	−0.083	0.00

Properties are reported only for three points along the BD annihilation path and for the unrelaxed geometries from TBMD simulations. See Ref. [27] for more details. ρ_b and $\nabla^2\rho_b$ in au

[117]. We have been able to find an evolutionary path from compact ($n < 5$) to elongated ($n \geq 5$) clusters and to explain this shape evolution using the atomic coordination, as determined by QTAIM, as a key parameter [28]. The average atomic coordination of the defective atoms increases linearly with n up to a maximal value of 6 for $n = 4$. Above this value, Si atoms appears to be unable to form new bonds, as also supported by the maximum average coordination of 6.5 observed in liquid silicon [118]. At this point, a new growth pattern has to start which eventually leads to the rod-like structures observed for extended defects [119].

4.2 Thermoelectric materials

Thermoelectric technology is currently employed in power generation and cooling system devices for specialized industrial and aerospace applications. To make one step further toward large scale applications is important since the energy-saving and environmental issues have becomes crucial in the perspective of compatible and sustainable growth [120,121].

TE devices are solid state cooling or power generators based on the TE effect, essentially made by one or more thermocouples that use two dissimilar TE materials [31,122]. Their figure of merit ZT,

$$ZT = TS^2\sigma/(\kappa_e + \kappa_L) \tag{8}$$

determines the efficiency of the devices, where S is the Seebeck coefficient, σ the electric conductivity, and κ_e and κ_L are the electronic and lattice contributions to the total κ thermal conductivity [122]. Best TE materials have ZT around 1.2, but competitive large scale TE applications would require materials with $ZT > 3$ [120].

The main efforts of the TE scientific community are currently focused on the search and the optimization of novel high-performance TE materials, which represents an extraordinary challenge in materials solid state chemistry [121]. Indeed, a significant ZT increase would mean to achieve simultaneously high $S^2\sigma$, typical of doped semiconductors, and low κ, typical of amorphous or ceramic materials.

As mentioned in Sect. 1, we have recently been involved in a European Community cooperative project aimed at developing nano-engineered high performance TE materials and devices. In the course of the project, almost all of the new promising TE materials have been considered [123]. In the following, we review our contribution to the research for improved and modified Co_4Sb_{12} skutterudite phases and Zn–Sb alloys using a chemistry-oriented approach first-principles modeling of novel TE materials [36]. Our work on type I inorganic clathrates $A_8Ga_{16}Ge_{30}$ (A=Sr,Ba) has been recently summarized [26] and it is thus not discussed here. We just mention that structural chemists generally regard these clathrates as Zintl phases, in which the guest atoms completely transfer/accept valence electrons to/from the framework [124]. This belief is firmly supported by the observation that all known clathrate type I structures exhibit a common number of 184 valence electrons per unit cell, despite the large number of elemental compositions forming these structures. However, studies on the very promising $A_8Ga_{16}Ge_{30}$ (A=Sr,Ba) TE materials, based on theoretical EDD [125] or maximum entropy method (MEM) analysis of experimental EDD [126], had questioned the ionic character of the guest atoms and rather propped up the idea of their almost neutrality. By describing the guest atoms as highly ionized species, our QTAIM analysis [37] could reconcile theory with

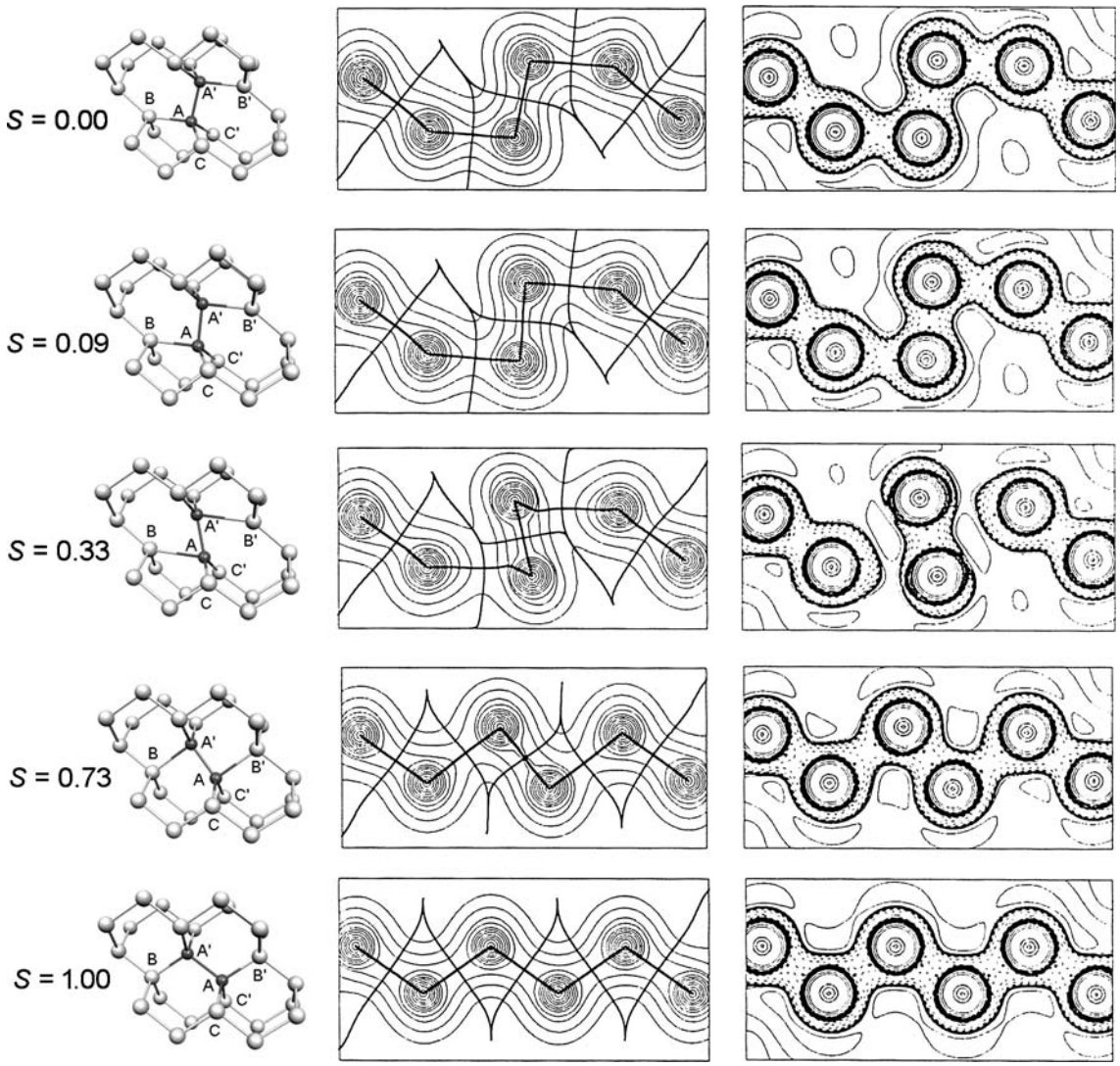

Fig. 7 The Bond Defect (BD) annihilation path. *Left* Stick-and-ball representation of the BD complex along the reaction path s for its annihilation. $s = 0$: BD complex; $s = 1$: non-defective crystal. The Si atoms connectivity is that obtained from the QTAIM analysis. *Middle and Right* Contour plots (AA′BB′ plane) of $\rho(\mathbf{r})$ and $\nabla^2\rho(\mathbf{r})$. Atomic interaction lines and boundaries are superimposed on the electron density plots. The bonded charge concentrations (BCC) are denoted by dots in the $\nabla^2\rho$ map. Adjusted from Figs. 2 and 3 with permission from Ref. [27]

the Zintl phase picture of these clathrates and with the role the guest atoms play as electron donors, according to the outcome of the density of states analysis of these compounds.

4.2.1 Modified Co_4Sb_{12} skutterudite phases

During the *Nanothermel* project considerable efforts have been devoted to the skutterudites phases. Binary skutterudites, Fig. 8, have general formula M_4X_{12} with bcc structure (space group Im $\bar{3}$). M is a transition metal, mainly from group VIII of the periodic table, X is a group XV element, and they occupy 8*c* and 24*g* crystallographic positions, respectively. The metal atoms form a cubic sublattice whose eight voids are partially occupied by six X_4 pnicogen rings. The 2*a* position, at the centre of the remaining two empty cubic voids, can by filled by loosely bound "rattling" atoms, affording the so called filled skutterudites phases. Among binary systems, Co_4Sb_{12} is attracting a considerable scientific interest [127]. This material is a narrow band-gap semiconductor, and it so represents a very good starting point material due to its excellent electronic transport properties. Nevertheless, the lattice contribution to its thermal conductivity is definitely too high (10 W/mK at room temperature, $ZT \approx 0.01$) for a high-performance TE

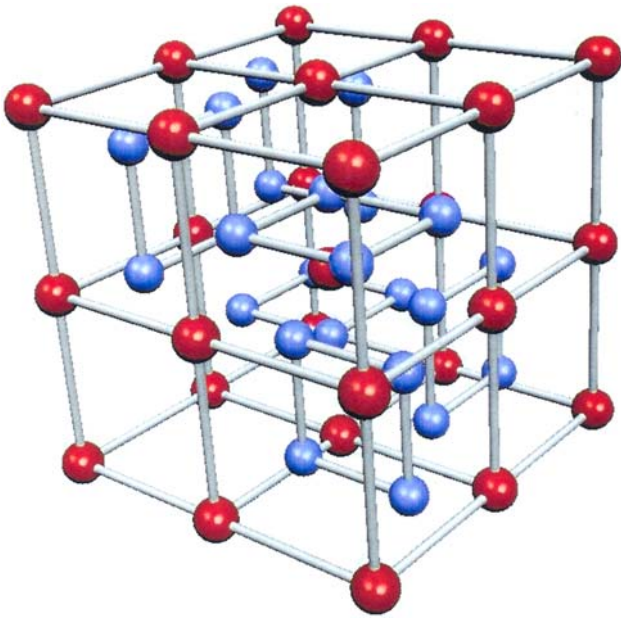

Fig. 8 The binary skutterudite structure M_4X_{12} (bcc structure, space group Im $\bar{3}$). *M* are transition metal atoms and *X* are pnicogen atoms. The metal atoms form a cubic sublattice whose eight voids are partially occupied by six X_4 pnicogen rings. The centre of the remaining two empty cubic voids can by filled by loosely bound "rattling" atoms, affording the so-called filled skutterudites phases

material and for this reason different structural modifications, like a *filling* with *interstitial* atoms of the empty cubic voids or a *substitution* in the frame or a suitable combination of these two changes, have been considered. The first modification seems to be the most promising. By filling cobalt antimonide, a drastic decrease of the thermal conductivity in a wide temperature range is generally observed [128,129] giving a higher ZT [130]. However, the filling generally lowers $S^2\sigma$, because it alters as well the carrier concentration of the system. Therefore, *frame* substitution is also introduced [131] for preserving reasonably good electronic transport properties.

Within this view, and in parallel to the synthetic and structural characterization efforts within the project, we performed an extensive computational work on several structural modifications of cobalt antimonide, as detailed in Table 8. In the following, we briefly review the main results in two simple key cases.

The Te-doped system is experimentally known to be a n-doped CoSb3 [132], but its TE properties should also depend on where the Te atom locates preferentially. Te atoms are expected to substitute the Sb atoms affording $Co_4Sb_{12-x}Te_x$, but they might also fill the cubic empty voids in the structure, providing the filled system $Te_xCo_4Sb_{12}$. Te substitution for Sb is hardly detectable by conventional X-ray diffraction (XRD) techniques, since the two elements have very similar scattering factors. We therefore evaluated [36,40,133] the geometrical and electronic structure for two model systems: a singly frame substituted ($Co_4Sb_{11}Te$) and a fully filled ($TeCo_4Sb_{12}$) Te-doped compound. As anticipated from n-doping, both systems were found to be conductors, while, as mentioned earlier, pure $CoSb_3$ is a narrow band gap semiconductor [134] with a direct band gap of 0.55 eV [135]. The optimized cell parameter for these compounds gave however a *first indication* as for the preferential location of the Te atoms in the structure. When Te replaces a Sb atom in 24 *g* position, the crystal undergoes a small increase of the cell parameter (+0.16%), in good agreement with the XRD estimate for a similar Te% content [132], whereas for a Te-filled crystal this increase is predicted about ten times as large [40,133]. When the total density of states (DOS), Fig. 9, and their atomic projections on the Te atom are inspected [40,133], one also notices remarkable differences in the electronic structure of the two studied compounds. In the filled system, the Te states fill up the band gap zone of the parent $CoSb_3$ compound and the Fermi level energy slightly decreases, while in $Co_4Sb_{11}Te$ the Te states are found to lie at the same energy of the Sb states they replace, thereby leaving the band gap zone of the parent compound almost unchanged. The Fermi level rises in energy in this case, affording a n-doped material as found experimentally. This provided a second *indication* as for the actual structure of the Te-doped system. Band by band analysis of the separate atomic contributions from Co, Sb, Te atoms to the bands in a region around the Fermi level quantitatively confirmed [40,133] the totally different role played by the Te atom when placed in the cubic voids rather than in the pnicogen rings. Calculation of electronic transport properties for the two systems provided a *third* clear *indication* for the preferential location of Te at the 24*g* position. Indeed, the computed Seebeck coefficient for $Co_4Sb_{11}Te$ is negative and it increases in magnitude almost linearly with T (see Fig. 9), in agreement with the available experimental findings [136]. On the contrary, in the filled system the S values are much lower in magnitude, close to zero in a large interval of temperatures (400–1,000 K) and even positive below 400 K (Fig. 9). This discussed case, as well as those we reported on the Sn, Ba and La-doped cobalt antimonides [35], provided a clear demonstration that the computed trends of S *versus* T may be used as a precious tool to distinguish among possible structural hypotheses upon doping [35]. Or, as we showed [35,137,138] in the case of the La- or Ca-doped systems where the dopant locates only in the cubic voids, that the solubility in $CoSb_3$ of the filler is most likely much

Table 8 Investigated structural modifications of cobalt antimonide

Where	Dopant	Position	Reference
Frame	Ni	8*c*	[36,39,40,139]
	Fe	8*c*	[39,138]
	Te	24*g*	[36,40,133]
	As	24*g*	This paper
	Sn	24*g*	[35]
	Ni and Te	8*c*, 24*g*	[40]
	Sn and Te	24*g*	Unpublished
Cubic voids	La	2*a*	[35,36]
	Ni	2*a*	[39]
	Ba	2*a*	[35,36,138]
	Sr	2*a*	[138]
	Te	2*a*	[36,133]
	Fe	2*a*	Unpublished
	Sn	2*a*	[35]
	Ca	2*a*	[137,138]
Frame and cubic voids	Ba, Ni	2*a*, 8*c*	Unpublished
	La, Ni	2*a*, 8*c*	Unpublished
	Ni, Ni	2*a*, 8*c*	Unpublished

In the parent, unsubstituted, $CoSb_3$ compound 8*c*, 24*g* represent the Wickoff positions where Co and Sb are, respectively, located. The filler atoms are introduced in the 2*a* positions located at the centre of the empty cubic voids. The dopant is(are) the element(s) replacing Co and/or Sb or the element filling the empty 2a positions. In most cases, more than one stoichiometry has been considered. For instance, all the four $Co_{4-x}Ni_xSb_{12}$ (x=1–4) systems were studied when Co was substituted by Ni (first entry in this table)

smaller than claimed experimentally. Finally, using the maximum power factor $S^2\sigma$ criterion and the frozen band approach, we evaluated the optimum Te doping for substitution at 24*g* position and found it dependent on T ($x = 0.5$ and 0.625 at 300 and 700 K, respectively) [133].

The second example concerns the combined use of synchrotron and neutron powder diffraction in tandem with ab initio calculations to solve the puzzle of the actual structure of the Ni-doped cobal antimonide [39] synthesized during the Nanothermel project. Knowledge of the precise structure is a prerequisite for any rational design of improved materials, but this has not been that easy for this class of compounds [39]. First, the key problem in the X-ray structural analysis of Co_4Sb_{12} samples containing Ni is the very similar scattering power of the transition metals, which makes it difficult to locate the dopant atoms in the structure. In addition, Co-containing samples give rise to strong fluorescence when measured at conventional powder diffractometers equipped with CuKα radiation sources. On top of this, Sb dominates the scattering relative to the transition metals. The sum of these factors makes the evaluation of the structure complicated at the conventional X-ray sources. In the case of neutron diffraction, there is a much higher contrast in the scattering lengths, Co (2.49 fm) and Ni (10.3 fm). But the peak resolution in the neutron diffraction experiment are often low compared with the conventional X-ray experiments and certainly lower than that of synchrotron experiments. In summary, a combination of neutron and X-ray diffraction gave complementary information, which could not be obtained from a single technique alone. Even so, structural questions emerged that called for information from additional sources to be properly answered. This was one of the reason behind our study [39,139] on frame substituted Co_4Sb_{12} systems with increasing Ni content ($Co_{4-x}Ni_xSb_{12}, X = 0 - 4$) and on the system with an interstitial Ni atom at the 2*a* special position, $NiCo_4Sb_{12}$. Indeed, the Rietveld co-refinement of the measured diffraction patterns obtained with conventional, synchrotron and neutron powder diffraction on $Co_{2.8}Ni_{1.2}Sb_{12}$ and using three different structural/composition models, gave support to the existence of two phases in such a sample [39]. However it left some unsolved questions as to whether the stoichiometry of the two phases is $CoSb_3$ and $NiSb_3$ or a mixture of a Co-rich, $Co_{4-x}Ni_xSb_{12}$ and a Ni-rich, $Co_yNi_{4-y}Sb_{12}$, phase. Furthermore each of the two phases might have contained both Ni substitution in the Co framework and Ni doping in the void. We hypothesized several model structures and calculated their Seebeck coefficients using the band structures relevant to these structural hypotheses. We were able to rule out the hypothesis of pure $CoSb_3$ and $NiSb_3$ phases and could demonstrate that the material is a mixture of a Co-rich and a Ni-rich phase, and with most of the Ni into the cubic frame, since a large amount of Ni in the voids would have exceedingly lowered $|S|$. Combining our theoretical results with spatially resolved Seebeck measures

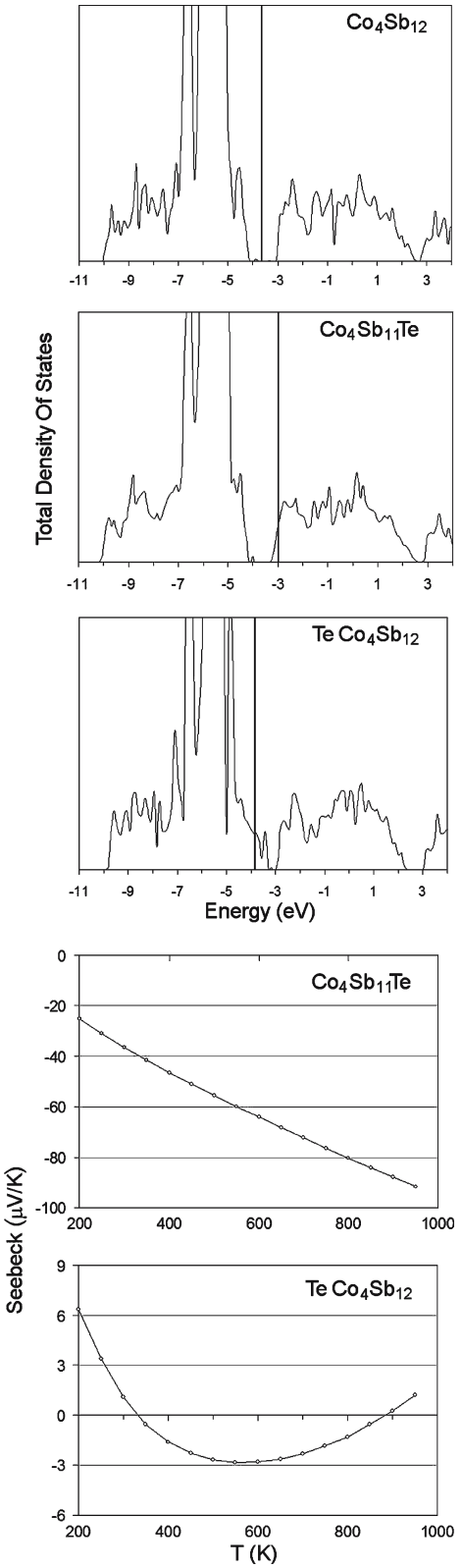

Fig. 9 Te-doped systems. Total DOS and Seebeck coefficients as a function of the absolute temperature T in the Te-doped cobalt antimonide. For the sake of comparison, the total DOS of the parent Co_4Sb_{12} compound is also shown (*top panel*)

we could also affirm that the Co-rich and the Ni-rich phases probably have similar x and y values and not far from 1. Full details on this study can be found in Ref. [39].

Currently, our work is proceeding along two main lines. On the one hand, the study of ternary skutterudite phases, and, on the other hand, the careful assessment of how the ab initio modeled transport properties are affected by the selected computational level [137,138].

Besides doping or nanostructuring, the lattice thermal conductivity of binary skutterudite can be reduced forming a ternary phase [140], with little effects on the electronic transport properties. Ternary skutterudite phases are obtained by substitution of 8*c* and/or 24*g* positions in a binary system and with the constraint of a constant number of valence electrons. There are mainly two types of ternary phases, the $Z+1/Z-1$ substituted ones (e.g. $Fe_2Ni_2Sb_{12}$ or $Co_4Sn_6Te_6$) and those obtained from same-group atom substitutions (e.g. $Co_4As_6Sb_6$). These phases are of great interest, since a ternary skutterudite phase has on average a thermal conductivity decreased by about 50–60% with respect to the corresponding binary system [141]. The current belief is that such a decrease is caused by the mass fluctuation induced by substitution, which would enhance the glass-like character of the material. We are studying the $Co_4Sb_6As_6$ skutterudite ternary phase to explore whether the charge transfer induced by substitution within the pnicogen rings—with the constraint of a constant number of electrons—can also play a significant role in diminishing k_L. Indeed, charge transfer may significantly affect the energy distribution of the phonons related to the Sb_4 rings normal modes, which are known to be the main responsible for the lattice thermal conductivity in the parent $CoSb_3$ compound [142].

As for the effect of the computational approach on the ab initio modeled electronic transport properties, we have selected the fully filled $CaCo_4Sb_{12}$ system as a suitable test case [137,138]. Results are currently being scrutinized against the atomic basis set quality, the DFT functional form and the kind of reference band structure used to obtain the optimal doping level within the frozen band approach. For the selected test case, the LDA, double ζ basis set level approach appears as a reasonable compromise between accuracy and computational cost. The trends of Seebeck coefficients are generally in good agreement with experiment, with the computed values at 300 K differing only within few percent from the experimental values at low filling fractions. Such an agreement is obtained only if the band structure of the filled system is adopted in the rigid band calculation, even at the low filler contents.

4.2.2 Zn–Sb alloys

The TE properties of Zn–Sb alloys are very promising, and strongly depend on the specific phase and exact composition. The β phase, whose formal stoichiometry is Zn_4Sb_3, attracted many investigations because it combines an exceptionally low thermal conductivity with the electronic transport properties of a p-doped semiconductor [143]. Its crystal structure remained an unsolved issue until recently, when it was solved by *Nanothermel* partners combining single-crystal X-rays [144] and powder-synchrotron-radiation diffraction methods plus Maximum Entropy analysis [38]. This structural study has shown how the existence of amorphous like, interstitial zinc atoms inside the rigid crystalline lattice can explain the very low lattice thermal conductivity of β-ZnSb [144]. Moreover, the discovery of such interstitial atoms gave for the first time a crystal structure of Zn_4Sb_3 consistent with the measured mass density. According to the powder diffraction (PD) results, Sb atoms sit in 6*e* and 4*c* positions of $R\bar{3}c$ space group (trigonal setting) with unit occupancy, while the Zn atoms are distributed with fractional occupancies over four 12*f* positions, from now on indicated with the capital letters A–D. The occupancy of one of the zinc sites is much larger than that of the other: A=0.899, to be compared with 0.068, 0.068 and 0.033 for B, C and D, respectively. The resulting overall stoichiometry is $Zn_{12.816}Sb_{10}$, which is zinc-deficient with respect to the formal 4:3 ratio.

We used an ab initio computational approach to *deconvolute* structural information from the *space–time* data averaging inherent to the PD experiment. As will be described below, this study enabled us to unravel the cell structures composing the material, and permitted us to evaluate which role the interstitial Zn atoms play in determining the electronic structure and transport properties of Zn_4Sb_3. Finally, we computed and rationalized the extreme sensitivity of the electron transport properties of this alloy to subtle changes in its composition. It is worth noting that the only ab initio study [145] on this subject available at the time of our investigation was based on an incorrect crystal structure, with no evidence of interstitial zinc atoms [146]. As a consequence, this theoretical study unavoidably missed the most important electronic features of the material, and described it as a low carrier density metal instead of a p-doped semiconductor, as found experimentally. The results of our investigation are summarized below, and have been extensively described in Refs. [36,38].

We computed the wave function of more than 100 different cell structures, by varying the location and number of Zn atoms within the experimental sites. The energy data have been analyzed to determine the local environments of Zn atoms whose mixing reproduces the experimental stoichiometry and minimizes the total energy of the material. Zinc antimonide consists of an ideal $A_{12}Sb_{10}$ framework where point defects distribute (see Fig. 10), in agreement with the experimental occupancy of the A site, which is much larger than B, C and D sites. Atoms in B and C positions are always coupled together to form dimers with a Zn–Zn distance of 2.23 Å. They occupy the cavity of a single A vacancy, and the clustering of dimers is disfavored. Atoms in D position reveal that the BC dimers possibly induce a rearrangement in their surrounding, by displacing zinc atoms from A to D positions to afford more complex structures of slightly higher energy. The experimental stoichiometry is exactly reproduced, assuming that the material is a 0.184:0.420:0.396 mixture of $A_{12}Sb_{10}$, $A_{11}BCSb_{10}$ and $A_{10}BCDSb_{10}$ cells, respectively. We found that cells with zinc content higher than 13 or lower than 11 zinc atoms are not energy competitive.

As concerns the electronic structure of this material, the $A_{12}Sb_{10}$, $A_{11}BCSb_{10}$ and $A_{10}BCDSb_{10}$ crystals appear to share very similar DOS patterns, as shown in Fig. 10. However, crystals with $Zn_{12}Sb_{10}$ stoichiometry ($A_{12}Sb_{10}$) are semiconductors with a p-doping level of two electrons per cell, and the insertion of another zinc atom in each cell ($A_{11}BCSb_{10}$ and $A_{10}BCDSb_{10}$) completely fills the gap. We could thus affirm that a mixing of cells with 12 and 13 zinc atoms such as to reproduce the experimental stoichiometry would produce a p-doped semiconductor, as found experimentally [143]. We then computed the electronic transport properties of ZnSb as a function of the zinc content, using the ELTRAP code. Given their similar DOS, we could model a variable stoichiometry of the material either by n-doping the 12-Zn atom cell or by p-doping one of the two 13-Zn atom cells, within the frozen band approximation. Regardless of the adopted band structure, we found that the experimental stoichiometry nearly corresponds to the optimal doping for the system, as estimated as the one yielding maximum power factor $S^2\sigma$. We concluded that interstitial zinc atoms do the trick in the β phase of zinc-antimonides. On the one hand, they act as electron suppliers and thus strongly enhance the Seebeck coefficient of the material [38]. On the other hand, they are point defects, thereby providing an efficient scattering mechanism for the phonons [144], which make them also responsible for the exceptionally low thermal conductivity of the material. Both effects concur to the increase of the figure of merit, ZT, of the material.

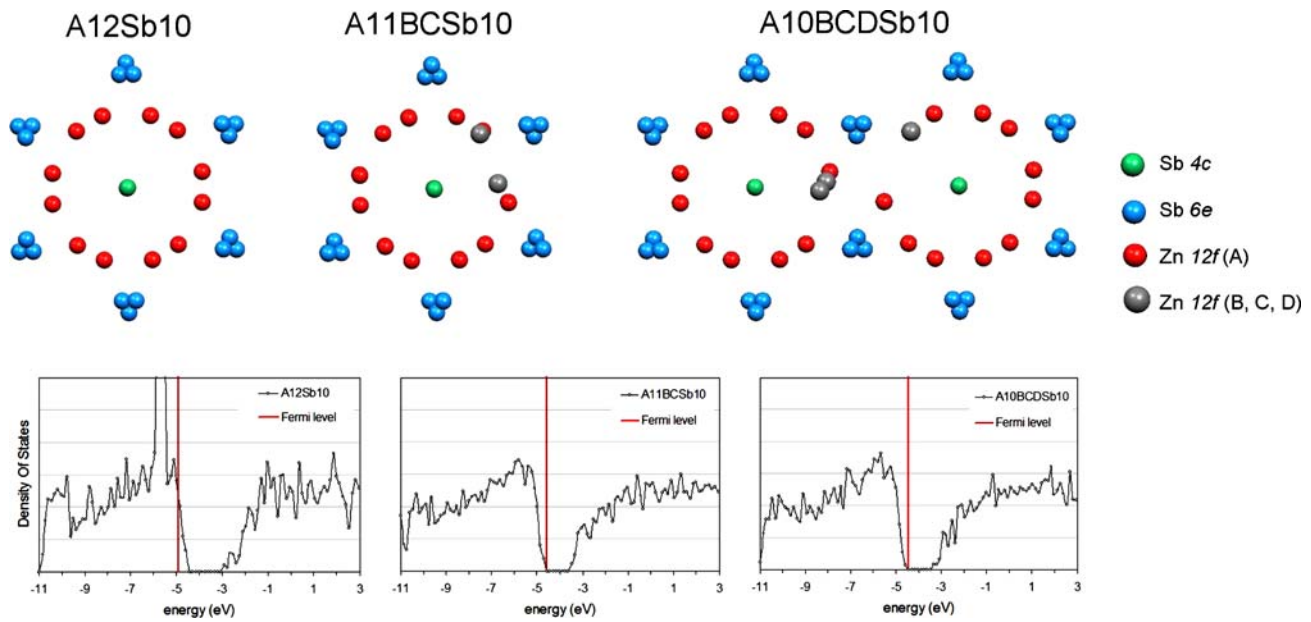

Fig. 10 The β-ZnSb alloy. *Top panels* atomic structure of the building blocks of the β-ZnSb alloy. *Left* the ideal $A_{12}Sb_{10}$ matrix; middle: a BC dimer substitutes an A type atom; *right* the BC dimer rearranges, displacing a Zn atom from A to D positions. *Bottom panels* DOS of the three structures

5 The Source Function and its application to molecular complexes

The SF, which has been introduced at the end of Sect. 1, is reviewed in its mathematical aspects, physical meaning and potential chemical use in Sect. 5.1. Recent applications of the SF analysis to the H-bonded complexes and to the *d*-block organometallic compounds are summarized in Sect. 5.2. A mention to the current and future developments of the SF concludes Sect. 5.

5.1 The Source Function

Few years ago, Richard Bader and one of us (CG) showed [2] that the electron density at any point **r** within a system may be regarded as consisting of contributions from a local source LS(**r**,**r**′), which operates at all other points of the space:

$$\rho(\mathbf{r}) = \int \mathrm{LS}(\mathbf{r},\mathbf{r}')\mathrm{d}\mathbf{r}' \tag{9}$$

The local source is given by $\mathrm{LS}(\mathbf{r},\mathbf{r}') = -(4\pi|\mathbf{r}-\mathbf{r}'|)^{-1} \cdot \nabla^2\rho(\mathbf{r}')$, where $(4\pi|\mathbf{r}-\mathbf{r}'|)^{-1}$ is a Green's function or, more simply, an *influence function* [147], representing the effectiveness of the *cause* $\nabla^2\rho(\mathbf{r}')$ to give rise to the *effect* $\rho(\mathbf{r})$. The integral of LS(**r**,**r**′) over the basin Ω of an atom (or group of atoms), $S(\mathbf{r},\Omega) = \int_\Omega \mathrm{LS}(\mathbf{r},\mathbf{r}')\mathrm{d}\mathbf{r}'$, has been termed the SF contribution, $S(\mathbf{r},\Omega)$, from that atom (or group of atoms) to $\rho(\mathbf{r})$ and it is thus a measure of the relative importance of its (their) contribution to the density at any point. One may so visualize the electron density at a point within a given basin Ω as determined by an internal SF self-contribution and by a sum of SF contributions from the remaining atoms or groups of atoms within a molecule, Eq. 10,

$$\rho(\mathbf{r}) = \mathrm{S}(\mathbf{r},\Omega) + \sum_{\Omega'\neq\Omega} \mathrm{S}(\mathbf{r},\Omega') \tag{10}$$

a decomposition which allows one to view the properties of the density from a new perspective and which foresees the SF as a tool able to provide interesting chemical insight [50].

The easiest way to derive the expressions for the SF is through the use of Green's theorem, $\int_A(\mathrm{u}\nabla^2 v - v\nabla^2\mathrm{u})\mathrm{d}\mathbf{r}' = \oint_{S_A}\mathrm{d}\mathbf{S}\cdot(\mathrm{u}\nabla v - v\nabla\mathrm{u})$, where A is an arbitrary basin and S_A its enclosing surface. Making the identifications, $\mathrm{u} = (|\mathbf{r}-\mathbf{r}'|)^{-1}$ and $v = \rho(\mathbf{r}')$, and exploiting the known [147] identity, $\nabla^2(|\mathbf{r}-\mathbf{r}'|)^{-1} = -4\pi\delta(\mathbf{r}-\mathbf{r}')$, and finally imposing the QTAIM zero-flux recipe $(\nabla\rho(\mathbf{r})\cdot\mathbf{n}(\mathbf{r}) = 0,\ \forall\mathbf{r}\in S_A)$ to get rid of the surface term $\mathrm{u}\nabla v$, one arrives to the expression given below:

$$\rho(\mathbf{r}) = -(1/4\pi)\left\{\int_A \frac{\nabla^2\rho(\mathbf{r}')}{|\mathbf{r}-\mathbf{r}'|}\mathrm{d}\mathbf{r}' + \oint_{S_A}\mathrm{d}\mathbf{S}(\mathbf{r}_S)\bullet\nabla|\mathbf{r}-\mathbf{r}_S|^{-1}\rho(\mathbf{r}_S)\right\} \tag{11}$$

In Eq. 11, the electron density at a point **r** within A is equated to the sum of two contributions, the first of

which is obtained by averaging the local source within A and the second is given by the flux of the electric field generated at $\mathbf{r}$ by the electron density on the surface boundaries of A [2]. For an isolated molecule or a molecular complex, A may be taken as the whole space and Eq. 11 can be easily rewritten in the form given by Eq. 10, for the electron density vanishes at infinity in this case and so does the surface integral contribution. Conversely, Eq. 11 is to be used for systems made of an infinite number of atoms, like the crystals, which have no boundaries at infinity. Or it may be exploited for large molecular systems to replace the integration of $\mathrm{LS}(\mathbf{r},\mathbf{r}')$ over all atoms of the system with just one basin and one surface integration.

Using the local expression [6] of the virial theorem, $1/4\nabla^2\rho(\mathbf{r}) = 2G(\mathbf{r}) + V(\mathbf{r})$, one may express [149] the local source as in Eq. 12

$$\mathrm{LS}(\mathbf{r},\mathbf{r}') = -\frac{1}{\pi}\frac{2G(\mathbf{r}) + V(\mathbf{r})}{|\mathbf{r}-\mathbf{r}'|} \tag{12}$$

which discloses a simple physical interpretation of LS, namely that to be related to the failure to locally satisfy the virial relationship between twice the kinetic and the virial field energies [$2\,G(\Omega) = -V(\Omega)$ for any basin defined through the QTAIM zero-flux recipe in a system at electrostatic equilibrium]. Equation 12 shows that the regions in a system where the electron density is concentrated ($\nabla^2\rho(\mathbf{r}')<0$) and where the potential energy dominates over the kinetic energy act as a *source* for the electron density at a point $\mathbf{r}$. On the contrary, the regions where the electron density is depleted ($\nabla^2\rho(\mathbf{r}')>0$) and where the kinetic energy dominates over the potential energy act as a *sink*, i.e., these regions remove electron density from $\mathbf{r}$. The effectiveness of such an accumulation or removal at $\mathbf{r}$ is then related to the magnitude of the charge concentration or depletion at $\mathbf{r}'$, weighted by the influence function introduced above.

The SF may be investigated using any point $\mathbf{r}$ in a system as a reference point, with BCPs having been generally assumed as the least biased choice for points representative of bonding interactions. Normally, we found that the positive LS contributions from an atomic basin to the density at system's BCPs dominate over its negative contributions. However, we discovered a number of interesting cases (see Sect. 5.2) [49–51], where an atom or group of atoms act as a sink rather than a source for the density at given system's BCPs. Clearly, for an isolated atom, the SF contribution to any point $\mathbf{r}$ must be always positive by definition.

The SF has so far been applied in relatively few cases [2,50–52,148,149] and most of its potentialities are probably still to be discovered.

For instance, the SF seems to provide a very sensitive measure of an atom's or chemical group's transferability and of the consequences derived thereof [2,50]. In fact, the density decomposition afforded by Eq. 10, reveals that the "perfect" transferability of a group property from one molecule to another not only implies that the corresponding group's electron density be transferable, but also that the sum of contributions to this density from the remaining atoms or group of atoms in the system remain constant. This is nicely illustrated by the SF analysis of the contributions to the electron density at the BCP for the unique C–H bond in a methyl group in n-alkanes, which was performed for the ethane, propane, butane and pentane series [2]. As it is well known [6], the terminal methyl group in n-alkanes, past ethane, is characterized by very transferable atomic properties, like the energy, the electron population, the volume and the spectroscopic properties regardless of the length of the chain. The transferability of the electron distribution in the methyl group is so good that a constant value for ρ_b at its unique C–H bond is also observed. When this value is analyzed in terms of the SF group contributions, one finds two important results. Namely: (a) the contribution from the atoms in the methyl group to ρ_b are constant at 0.270 au throughout the investigated series, with the contribution from the two equivalent methyl groups hydrogens to this amount equaling 0.0210 au in all four molecules, and (b) the constancy in the ρ_b value (0.283 au) for the terminal C–H bond is a result of a constancy in the sum of the source contributions to ρ_b from the groups external to the methyl group, *regardless of the length of the chain*. Thus the ethyl group in propane contributes the same as the propyl group in butane, which in turn contributes the same as the butyl group in pentane. This effect is more than a simple fall-off in the source contribution with each additional group, since the value of the SF contribution for each succeeding increment is predetermined, as it must equal the contribution from the H atom it replaces.

The study of the series Li–X (X = F, O, N, Cl, H) provided an interesting case of how sensitive to the actual extent of chemical transferability is the SF indicator [50]. The Li atom in this series is known to exhibit nearly constant and transferable properties, including its net charge and atomic energy [6]. Therefore, in the limit of perfect transferability, the SF contribution from Li at the BCP should remain constant along the series, with the observed changes in the ρ_b values be simply determined by correspondingly equal changes in $S(\mathbf{r}_b, \mathrm{X})$. Instead, Table 9 shows that not only the ρ_b value but also the contribution to this value from Li, $S(\mathbf{r}_b,\mathrm{Li})$, decreases by a factor of about two along the series. This proves $S(\mathbf{r}_b,\mathrm{Li})$ to be a more sensitive index of a departure from perfect

transferability than are the integral averages yielding the atomic population and energy (Table 9). By inspecting the profiles of $S(\mathbf{r},\mathrm{Li})$ along the Li–X axis, we could demonstrate that the Li atom gives a constant contribution to $\rho(\mathbf{r})$ for any X, up to a distance of 0.58 Å from the Li nucleus (Fig. 3, Ref. [50]), a distance which almost corresponds to the closest BCP from the Li nucleus in the series (X = F, Table 9). The observed changes in $S(\mathbf{r}_b,\mathrm{Li})$ are therefore just a consequence of the progressive shift of the BCP towards the X nucleus along the series. Besides the recognition of the extreme sensitivity of $S(\mathrm{r},\Omega)$ to chemical transferability, another interesting result came out from this study [50]. We found out that the percentage contributions from Li to ρ_b remains almost constant throughout the series, at about 40% (Table 9). Therefore, rather than to be reflected in a constant source contribution, the clear cationic nature of Li throughout the series [see N(Li) values, Table 9) manifests itself as a constant *percentage* SF contribution from Li to ρ_b. The shift in the BCP location along the series just serves to ensure the constancy of this percentage contribution.

We have also shown that the SF contributions to the density at a BCP reflect the nature of the associated chemical bond.[10] Figure 11 (top) displays such contributions for two very simple cases, the C–C BCP in the ethane, ethylene and acetylene series [52] and the B–H_{bridge} BCP in the much less localized context of the B–H_{bridge}-B 3*c*, 2*e* bonds in diborane [52]. In Fig. 11, each atom Ω is displayed as a sphere having a volume which is proportional to the SF percentage contribution from Ω to the electron density at the BCP which is denoted by a black dot. The CC bond is a well-known covalent bond and most of contributions to its ρ_b value come from the two bonded C atoms, which, for instance, account for about 80% of the ρ_b value in ethane, the remaining 20% coming from the H atoms. The percentage source contribution from the C atoms increases with increasing formal bond order and reaches a value of about 89 and 96% for ethylene and acetylene, respectively. As a consequence, the percentage contribution from the whole set of H atoms decreases along the series, and so does also the percentage source from each H atom, which diminishes from a value of 3.6% in ethane down to a value of 2.1% in acetylene. As one would expect from chemical knowledge, the SF describes the B–H_{bridge} bond as much less localized in nature [52]. The two connected atoms contribute to only 55% of the BCP density and their involvement in the bond is asymmetric, the largest percentage contribution (36%) coming from the hydridic H atom. The remaining 45% contribution, except a residual 10%, is almost equally shared among the other bridged H atom and each of the two terminal H bonded to the B atom. Surprisingly, the contribution from the other B atom is almost negligible, being less than 3%.

The delocalization index $\delta(\Omega,\Omega')$ expresses the amount of total (coulomb plus exchange) electron correlation shared between basins Ω and Ω′ and viceversa, and is thus a measure of the sharing of electrons pairs between Ω and Ω′ [48]. On account of this, $\delta(\Omega,\Omega')$ and SF contributions at BCPs are not physically related in a direct way. Nonetheless, we thought it worth examining whether empirical relationships among these quantities could be possibly observed [52]. In the case of diborane, H_{bridge} has an electron exchange with the other bridged H (δ = 0.214), or with the terminal H atom, (δ = 0.109), which is of the same order of magnitude of that with its bonded B atom (δ = 0.332). This is in line with the SF description. One also finds that the δ(C,C′) delocalization indices in the ethane, ethylene, acetylene series are as large as 1.03, 1.92 and 2.76, respectively. The higher $\delta(\Omega,\Omega')$ values for this series and their increase along the series comply with the higher SF percentage contributions to ρ_b from the two bonded atoms and with the trend of such contributions through the series. On the other hand, the electron exchange of C with a H linked to C′ is 1–2 order of magnitude lower (0.042, 0.062 and 0.062) than δ(C,C′), which also agrees with the low source contribution from H to the C–C BCP density.

Also shown in Fig. 11 are the percentage SF contributions in bis(pentacarbonylmanganese) at the $\mathrm{Mn-C_{equatorial}}$ and $(\mathrm{CO})_{equatorial}$ bonds [52]. The percentage contributions from Mn and C atoms to the Mn–C BCP are both positive, almost equal in value, and intermediate between those found for polar or non polar covalent bonds and for the B–H_{bridge} in diborane. The most important "external" contribution is from the O atom linked to the C (14%), the other atoms in the molecule supplying the remaining 19%. Despite the C–O bond has a positive, small $\nabla^2\rho_b$ value (0.8 au), the percentage sources from the two bonded atoms comply with this bond being strongly covalent and polar, as testified by the sum of sources being close to 100% and by the larger percentage source from the O (58%) compared to that from the C atom (40%). A quite different SF description is found for the metal–metal bond in this molecule (Sect. 5.2).

The SF analysis has also been applied to the HX (X = Li, Be, B, H, C, N, O, F) series [50]. Contrary to the case of the RC–H bond in n-alkanes, where the C–H group (and the terminal CH_3 group) gives a constant source contribution to the density at the terminal C–H BCP, one

[10] The case of H-bonds and of metal–metal bonds in *d*-block organometallic compounds is reviewed in the next section.

Table 9 Source function contributions to the BCP density in the LiX series

Li–X	$[R_e(R_{Li})]$(Å)	ρ_b	$S(\mathbf{r}_b, Li)$	$S(\mathbf{r}_b, Li)$ %	N(Li)	$-E$(Li)
Li–F	1.553 (0.597)	0.078	0.033	42.9	2.059	7.3419
Li–O ($^2\Pi$)	1.671 (0.622)	0.067	0.028	41.6	2.066	7.3467
Li–N ($^3\Sigma$)	1.840 (0.657)	0.054	0.022	39.9	2.075	7.3565
Li–Cl	2.035 (0.685)	0.045	0.018	39.8	2.065	7.3274
Li–H	1.608 (0.713)	0.040	0.016	40.0	2.086	7.3655

Data from Ref. [50]; N(Li) and E(Li) are the electron population and the atomic energy of Li, respectively. If not otherwise stated, all quantities in au. R_e is the equilibrium distance, while R_{Li}, reported in parenthesis, is the distance from the Li nucleus to the BCP

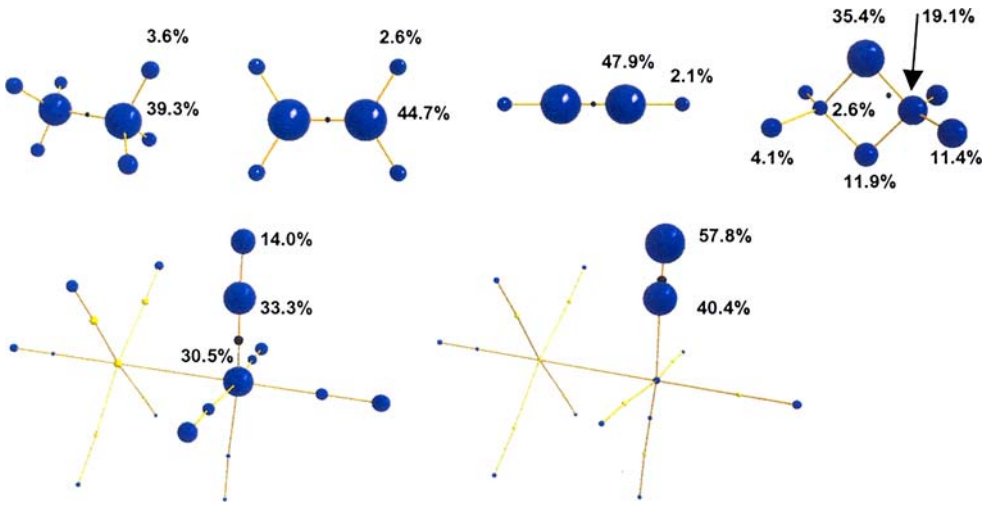

Fig. 11 Percentage SF contributions to the density at BCPs. The position of the selected BCP is denoted by a black dot. Each atom Ω is displayed as a sphere whose volume is proportional to the SF percentage contribution from Ω to the electron density at the indicated BCP. *Top* from left to right: SF percentage contributions to the density at the CC BCP in ethane, ethylene, acetylene and to the density at the B–H_{bridge} BCP in diborane. *Bottom* SF contributions to the density at the Mn–$C_{equatorial}$ and at the $(C–O)_{equatorial}$ bonds in bis(pentacarbonylmanganese) [Adjusted from Figs. 3 and 4 with permission from Ref. [52], Copyright 2007 by Royal Society of Chemistry]

expects that contribution from H to ρ_b will depend on the nature of X, if the SF is not just an elegant mathematical tool, but one bearing chemical information. Indeed, it was shown that the percentage SF contribution from H to ρ_b decreases with increasing X's electronegativity, and that this decrease is the result of significant changes in the Laplacian distribution within the H basin along the series.

Although customarily applied to the determination of density contributions at BCPs, the SF analysis may use as a reference point any point **r** in a system, including the nuclei and the NNAs [50]. Application of the SF to planar lithium clusters, which are characterized by the occurrence of NNAs and by the lack of any direct Li–Li BP [59], has revealed that the SF clearly distinguishes between a NNA electron density maximum and a maximum associated to a nucleus [50]. While the self-basin contribution is higher than 99.95% in the case of a normal nuclear attractor, this same contribution lowers to about 70% for a NNA in these clusters, with important contributions from the Li basins and from the basins associated to the other NNAs. The different chemical nature of these (3,−3) CPs is evidently put to the fore by the SF analysis.

Analysis of LS(BCP, $\mathbf{r}'$) profiles, with $\mathbf{r}'$ running along a BP, have been discussed for the series of second-row diatomic hydrides [51], for a number of hydrogen-bonded systems in the gas and crystalline phase [51], and for the metal–metal bonds in *d*-block organometallic compounds [52]. With respect to the integral form of the SF function, the study of its local form, LS(BCP, $\mathbf{r}'$), along a BP, introduces further detail. It allows to disclose which regions in the basins of the two linked atoms accumulate or remove charge at the BCP, as a function of the nature of the bond and of the external perturbations (substituent effects, crystal field, etc.) acting on this bond [51]. Or it enables one to unveils interesting differences in how the charge density originates at an A–A′ internuclear midpoint when the two atoms are linked by a BP or not [52].

5.2 Applications to the H-bonded molecular complexes and to the *d*-block binuclear organometallic compounds

The HB is known to exhibit an extraordinary variety of geometries and of dominating energetic contributions according to the nature of the H-donor and H-acceptor atoms [150]. The HBs energies, which extend from about 15–50 kcal/mol for strong bonds, down to 1–4 kcal/mol for the weak bonds, are evidence of a wider range of atomic interactions than is observed for covalent or ionic bonds or van der Waals forces [150]. Therefore, we thought that HBs could represent an interesting test to explore how the nature of an HB reflects in the SF contributions to the H-bond BCP density from the atoms directly involved in the HB (the H, the H-donor and the H-acceptor atoms) and from the remaining atoms in the HB complex.

We studied the case of the reaction path for the approach of two water molecules, as a first guide to understand how the SF contributions to the HB ρ_b value change with changes in the H-donor to H-acceptor distance and, hence, in the HB nature [50]. We then applied the same kind of analysis to two prototypical sets of H-bonded systems [50], one of which (Table 10 and Fig. 12) is enumerated below according to the HB classification put forth by Gilli and Gilli [151]. This set included: **1**, the symmetrical $[H_2O\cdots H\cdots OH_2]^+$ dimer, a positive Charge Assisted HB, (+)CAHB; **2**, the open form of the formic acid–formate anion complex, a negative Charge Assisted HB, (−)CAHB; **3**, malonaldeyde, in its C_s equilibrium form, a Resonance Assisted HB (RAHB); **5**, the cyclic homodromic water trimer, a Polarization Assisted HB, (PAHB); **6**, the water dimer at equilibrium geometry, an Isolated HB (IHB). Also listed in Table 10 and shown in Fig. 12 is **4**, the C_{2v} TS for the H-atom transfer between the two oxygen atoms in malonaldeyde. As shown in Fig. 12, the atomic percentage contributions change dramatically along this set of H-bond complexes. Only the global percentage contribution from either the H-donor (S_{MolD}%) or the H-acceptor molecule remain almost constant (Table 10) and not dissimilar from each other, for those systems where these two moieties can be identified. Also stable enough, and around 30–40% is the value of S(H+D)%, the percentage contribution from the H involved in the HB and the oxygen donor D. Its relative constancy, Table 10, denotes that, besides the donor and acceptor molecules, also D–H behaves to a some extent as an atomic "transferable" group. On the other hand, the percentage source contribution from the H, S(H)%, appears to be the *most distinctive marker* of the change of the H-bond nature along the reaction path. S(H)% is

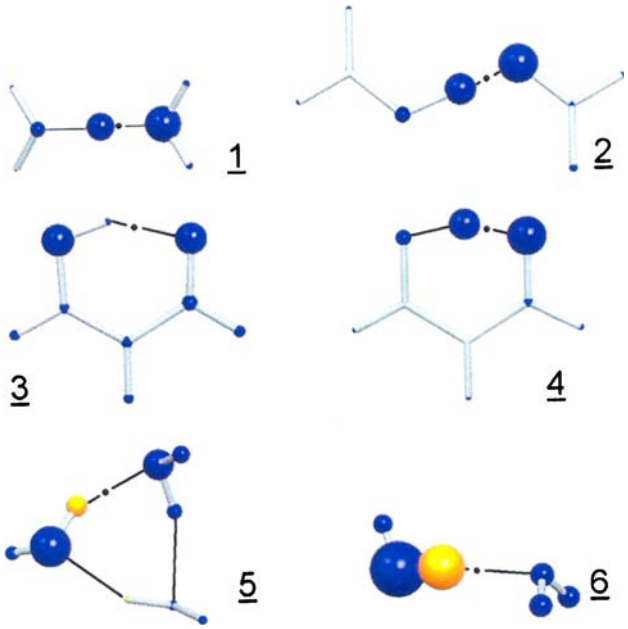

Fig. 12 Prototypical H-bonded molecular complexes: percentage atomic source contributions to the electron density at the HB critical point. Prototypical H-bonded systems: **1** $H_5O_2^+$; **2** open form of the formic acid–formate anion complex; **3** malonaldeyde, C_s equilibrium form and **4**, C_{2v} transition state for H-migration; **5** cyclic homodromic water trimer; **6** water dimer at equilibrium geometry. Positive sources in *blue* and negative sources in *yellow*. The *black dot* denotes the HB critical point for which the atomic source contributions are evaluated. (Adjusted from Fig. 7 with permission from Ref. [50], Copyright 2003 by Wiley Periodicals, Inc.)

positive and around 30% for the charge assisted HBs, positive but very close to zero for the RAHB system, **3**, which has a H-donor to H-acceptor $d_{D\cdots A}$ distance of about 2.5 Å . At higher $d_{D\cdots A}$ values, S(H)% becomes even negative, and as low as −72.3% in the water dimer. One may feel uncomfortable with such a result. However, the negative S(H) contribution is simply the consequence of a change into the shape of the H atom and into the Laplacian distribution within its basin along the series with increasing $d_{D\cdots A}$ distance. As this distance increases, the HB critical point moves away from the O–H negative Laplacian region (see Fig. 6, Ref. [50]) and it becomes surrounded by regions of positive Laplacian of increasing size and located within the H basin. Accordingly, the SF contributions from the H to the HB CP become negative and the more and more so, the larger is $d_{D\cdots A}$.

The percentage contributions from the H and the donor oxygen, S(H+D)%, or from the H and the acceptor oxygen, S(H+A)%, are generally much smaller (if not even negative) than found for normal covalent or dative bonds. This results from the H-atom behaving as a sink past moderately large $d_{D\cdots A}$ distances and as a modest

Table 10 Source function contributions at the H-bond CP in a number of prototypical H-bonded complexes

$d_{D\cdots A}$ (Å)	System, H-bond class	ρ_b	S(H)%	S(H+D)%	S(H+A)%	S(H+D+A)%	S_{MolD}%
2.41	**1**, +(CAHB)	0.167	31.4	41.0	83.1	92.7	43.5
2.43	**2**, −(CAHB)	0.167	32.1	40.4	82.0	90.3	43.8
2.37	**4**, RAHB*[a]	0.177	32.2	40.7	80.9	89.5	–
2.54	**3**, RAHB	0.056	2.1	36.8	36.1	70.8	–
2.75	**5**, PAHB	0.035	−14.4	38.7	16.6	69.7	–
3.02	**6**, IHB	0.016	−72.3	34.3	−53.7	53.0	47.6

Data from Ref. [50]; all quantities in au, except for $d_{D\cdots A}$, the distance between the H-donor and the H-acceptor atoms, which is given in Å. See the text and Fig. 12 for the H-bonded complexes numbering. Classification of HB (column 2) according to Ref. [151]. H,D and A are, respectively, the H directly involved in the HB, the H-donor and the H-acceptor atoms. S(H+D), S(H+A) and S(H+D+A)% are the sums of percentage SF contributions from H+D, H+A and H+D+A group of atoms, respectively. S_{MolD}% is the percentage SF contribution from the H-donor molecule, when this molecular moiety can be identified

[a] System **4** is classified as RAHB* since it corresponds to the transition state for the H atom migration in malonaldeyde (see the text)

source at $d_{D\cdots A}$ distances below 2.5 Å. Percentage values close to 85–90%, as found for covalent bonds, are obtained only when the sum of percentage contributions from all the three atoms directly involved in the HB, S(H+D+A)%, is considered, and only for $d_{D\cdots A}$ distances below 2.5 Å, where the three-center nature of HBs is thereby confirmed [151]. For larger distances, the contributions from atoms other than the triad directly involved in the H-bond become important, being about 30% for PAHB and RAHB bonds and as large as 47% for the IHB bond (Table 10). As the donor to acceptor distance increases, other atoms in the molecular complex become progressively involved in the H-bond (Fig. 12), in accord with the increasing electrostatic character of the interaction.

When the data for malonaldeyde are compared with those for the water trimer (Table 10), one observes that the RAHB complex **3** is characterized by an enhanced source contribution from atoms other than the H+D+A triad and by a decreased local character of the D–H and D–A interactions than expected on the basis of the donor–acceptor separation only, which is about 0.2 Å larger than in the PAHB system. A similar behavior occurs in the transition state for the H atom migration in malonaldeyde, **4**, which has more delocalized sources than the -CAHB system **2**, despite a smaller $d_{H\cdots O}$ distance than **2**. Clearly, the anomalies observed for systems **3** and **4** can be traced back to their RAHB nature.

We did also highlight an interesting parallel between the classification of HBs provided by the ELF topologic approach [152] and by the SF analysis. For instance, the advent of a valence monosynaptic H basin in the reduction of the ELF localization domains only occurs when the SF contribution from the H to the density at the H-bond CP is significantly positive. That is strong H-bonds, as classified by the ELF topological approach, comply with S(H)>>0. Further details on the comparison between the two topological classifications can be found in the original paper [50].

Our very recent work [52,153] on the metal–metal (M–M) bond in *d*-block binuclear organometallic compounds is aimed at exploring the kind of information the SF can provide on a bond which has kept challenging theory as for the detailed understanding of its nature in many transition molecular complexes [154]. It is now widely acknowledged [155–157] that many traditional bonding paradigms can no longer be applied to the M–M bonds and, even in the framework of the topological analyses of the chemical bond, it has become increasingly manifest that well-established bond classification schemes need to be critically reconsidered and revised when applied to these atypical bonds [1,46,155,157]. Indeed, the dichotomous classification based on the sign of $\nabla^2\rho_b$ is clearly inadequate [46] for bonds between atoms which miss the outermost regions of charge depletion and concentration in their atomic Laplacian distributions. Other quantities, which have been proposed as more suited topological indices for M–M bonds, all require the knowledge of the first (and second) density matrices, which are in general not directly amenable to experiment. These indices include the QTAIM delocalization indices [48], the $|V_b/G_b|$ ratio [90], the energy density H_b, the bond degree, H_b/ρ_b [90], the synaptic order and the population of ELF valence basins [45,49]. Conversely, the SF analysis permits to go one step further the conventional topological BCP indices directly derived from the EDD, but still making use of information contained only in $\rho(\mathbf{r})$ and without introducing any approximate formula . As such it might be rigorously applied also to charge densities obtained from experiment, if available.

Our preliminary study [52] has concerned three different series of *d*-block organometallic compounds with formal single or multiple M–M bond.

Figure 13 (top) shows the SF percentage contributions to the metal–metal bond in $Mn_2(CO)_{10}$, a system with a formal M–M bond order of one and whose bonding is still a matter of debate [157]. The Mn atoms act as a sink [S(Mn) = −25.0%] for the electron density at the Mn–Mn BCP and are the carbonyl groups, or more precisely, the carbonyl oxygen atoms that, thanks to their high positive sources at this BCP, outweigh the negative contribution from the two Mn atoms. The SF views the Mn–Mn bond as strongly not localized. The ligands play the role to polarize the atomic Laplacian distribution within the Mn basins in such a way as to make these atoms subtracting density rather than accumulating it at the Mn–Mn BCP. The negative SF(BCP,Mn) value complies with a δ(Mn,Mn′) value of 0.28, which is indeed very small for a formal single bond [δ (C,C′) = 1.03 in ethane, see earlier]. This value is comparable to that found between Mn and the axial or equatorial oxygen atoms [$\delta(\mathrm{Mn,O_{ax}}) = 0.22; \delta(\mathrm{Mn,O_{eq}}) = 0.17$], which are only indirectly (1,3) bonded to Mn through the corresponding carbon atoms.

Figure 13 also displays the SF contributions to the density at the Co–Co midpoint in two, apparently quite distinct cases: the unbridged $Co_2(CO)_8D_{3d}$ isomer, which is metal–metal bonded and the double bridged $Co_2(CO)_8C_{2v}$ isomer, which does not exhibit any Co–Co BCP [52]. In both systems the electron density at BCP or at the Co–Co midpoint is due to the carbonyl groups (and in particular to the oxygen atoms) and it is only the relative contributions from these groups that is varying between the two structures, with bridging carbonyl groups playing a major role in the C_{2v} form. In both complexes the percentage SF contribution from the Co is very close to zero and, surprisingly, slightly higher (0.7%) for the "non bonded" compound than is for the "bonded" isomer (−4.4%). Yet, inspection of the Laplacian and of the local source profiles along the Co–Co internuclear axis reveals that the two systems noticeably differ in the way the Co basin locally contributes to the density at the Co–Co midpoint. The similar source contributions from the Co atom in the two isomers is just the result of a compensation among different, characteristic contributions from the various regions of their basins. The analysis of the local source contributions reveals small but unequivocal signs of incipient covalency, in the bonded isomer, in a region close to the BCP [52].

As a general outcome of our study, we have found that the SF description of the M–M bonding along a series is closely related to that provided by the localization/delocalization indices. The agreement persists even when the M–M bond is lacking and the internuclear M–M midpoint is taken as a reference point for evaluating the SF contributions. However, use of the local form of the SF unveils interesting differences as of how the charge density originates at the M–M midpoint when the system is M–M bonded or not. We also found that most of the topological indices, which are conventionally adopted to describe M–M bonds fail in reproducing the expected chemical trends for the set of investigated systems, with the adimensional $|V_b|/G_b$ ratio and the $\nabla^2\rho_b$ value being particularly inadequate.

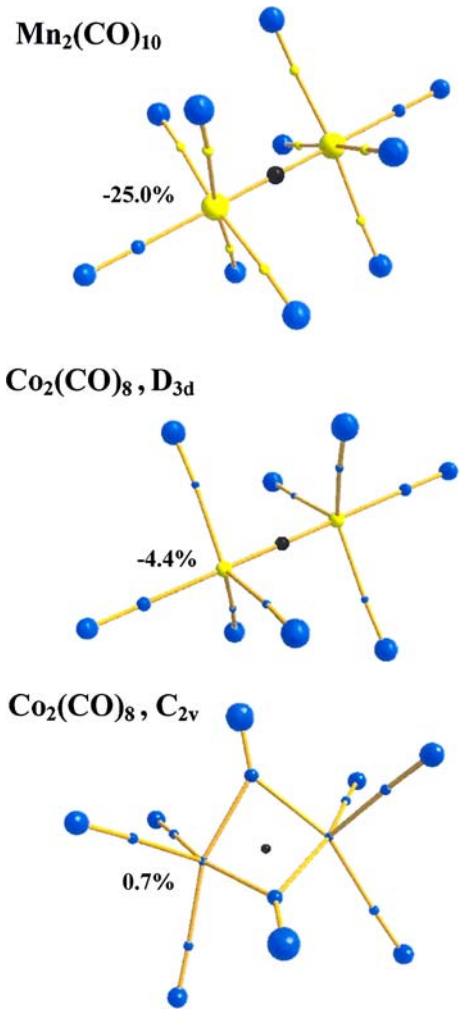

Fig. 13 Percentage SF contributions to the density at the internuclear metal–metal midpoint. From top to bottom: bis(pentacarbonylmanganese), the *bonded* $Co_2(CO)_8D_{3d}$ isomer, the *non-bonded* $Co_2(CO)_8C_{2v}$ isomer. Positive sources in *blue* and negative sources in *yellow*. The *black dot* denotes the point (BCP or metal–metal midpoint) for which atomic source contributions are evaluated. Metal percentage SF contributions are also reported as numerical values [Adjusted from Fig. 4 and Fig. 7 with permission from Ref. [52], Copyright 2007 by Royal Society of Chemistry]

5.3 Future developments

The applications of the SF analysis to crystalline systems have so far been limited to the study of the local source contributions LS [51] or to the incomplete use of the density decomposition afforded by Eq. 10, for only a finite number of contributions from external basins ($\Omega' \neq \Omega$) can obviously be evaluated. We are therefore currently implementing [158] the density decomposition given by Eq. 11, which, as mentioned earlier, is the proper expression to be used for systems made of an infinite number of atoms, or to be adopted as an expedient to replace the integration of LS(r, r′) over all atoms of the system with just one basin and one surface integration.

We are also making progresses [158] (D. Lasi and C. Gatti in preparation) in deriving an ambiguity-free full population analysis, based on the SF. This simply requires to integrate Eq. 10 (or Eq. 11) over a basin Ω. The resulting atomic electron population N(Ω) may so be decomposed[11] as: $N(\Omega) = M(\Omega,\Omega) + \Sigma_{\Omega' \neq \Omega} M(\Omega,\Omega') = N_{\mathrm{i}}(\Omega) + N_{\mathrm{o}}(\Omega)$, where the inner contribution, $N_{\mathrm{i}}(\Omega)$, and the outer contribution, $N_{\mathrm{o}}(\Omega)$, to $N(\Omega)$ are given by $N_{\mathrm{i}}(\Omega) \equiv M(\Omega,\Omega) = \int_{\Omega} S(\mathbf{r},\Omega)\mathrm{d}\mathbf{r}$ and by $N_{\mathrm{o}}(\Omega) \equiv \Sigma_{\Omega' \neq \Omega} M(\Omega,\Omega') = \Sigma_{\Omega' \neq \Omega} \int_{\Omega} S(\mathbf{r},\Omega')\mathrm{d}\mathbf{r}$, respectively. One can also define a shared population, $\mathrm{SP}_{\Omega\Omega'}$, between each pair of atoms Ω, Ω', as $\mathrm{SP}_{\Omega\Omega'} = M(\Omega,\Omega') + M(\Omega',\Omega)$, thus obtaining a full population analysis based only on the $\nabla^2\rho$ observable. Note that at variance with other schemes of population analyses, $M(\Omega',\Omega)$ has not to be necessarily equal to $\mathrm{M}(\Omega,\Omega')$. In spite of its simplicity, implementation of the SF derived population analysis is not straightforward since the SF decomposition of the density becomes numerically problematic whenever the value of the electron density to be reconstructed (Eq. 10 or Eq. 11) falls below 10^{-3}–10^{-4} au. This makes the partitioning among the inner and outer contributions very sensible to the quality of the electron density reconstruction in the low density regions [158]. In addition, this ambiguity-free population analysis is very CPU time consuming. However, we could already observe interesting correlations of $M(\Omega,\Omega)$ and $M(\Omega,\Omega')$ with, respectively, the localization and the delocalization indices in a number of diatomics and along the ethane, ethylene, acethylene series [158]. Clearly, this population analysis can potentially be also applied to the experimental electron densities.

Finally, we plan to extend the SF approach and the population analysis based on the SF to the α- and β-components of the spin-polarized densities.

[11] In the case one integrates Eq. 10. Integration of Eq. 11 affords an outer contribution expressed as a sum of contributions from each of the interatomic surfaces of Ω.

References

1. Gatti C (2005) Z Kristallogr 220:399–457
2. Bader RFW, Gatti C (1998) Chem Phys Lett 287:233–238
3. Destro R, Marsh RE, Bianchi R (1988) J Phys Chem 92:966–973
4. Destro R, Bianchi R, Gatti C, Merati F (1991) Chem Phys Lett 186:47–52
5. Coppens P (1997) X-ray charge densities and chemical bonding. IUCr texts on crystallography 4. Oxford University Press, Oxford
6. Bader RFW (1990) Atoms in molecules: a quantum theory. International series of monographs on chemistry 22. Oxford University Press, Oxford
7. Gatti C, Bianchi R, Destro R, Merati F (1992) J Mol Struct (THEOCHEM) 255:409–423
8. Coppens P (1998) Acta Cryst A 54:779–788
9. Dovesi R, Saunders VR, Roetti C, Causà M, Harrison NM, Orlando R, Aprà E (1996) CRYSTAL95 User's Manual, University of Torino, Torino
10. Gatti C (1999) TOPOND-98: An electron density topological program for systems periodic in N (N=0–3) Dimensions, User's Manual, CNR-ISTM, Milano
11. Volkov A, Gatti C, Abramov Y, Coppens P (2000) Acta Cryst A 56:252–258
12. Koritsanszky T, Richter T, Macchi P, Volkov A, Gatti C, Howard S, Mallinson PR, Farrugia L, Su Z, Hansen NK (2003) XD: Computer program package for multipole refinement and topological analysis of electron densities from diffraction data
13. Gatti C, Saunders VR, Roetti C (1994) J Chem Phys 101:10686–10696
14. Gatti C, May E, Destro R, Cargnoni F (2002) J Phys Chem A 106:2707–2720
15. May E, Destro R, Gatti C (2001) J Am Chem Soc 123:12248–12254
16. Gatti C, Silvi B, Colonna F (1995) Chem Phys Lett 247:135–141
17. Aray Y, Gatti C, Murgich J (1994) J Chem Phys 101:9800–9806
18. Jeffrey GA (1999) J Mol Struct 485–486:293–298
19. Bianchi R, Gatti C, Adovasio V, Nardelli M (1996) Acta Cryst B 52:471–478
20. Volkov A, Abramov Y, Coppens P, Gatti C (2000) Acta Cryst A 56:332–339
21. Hibbs DE, Overgaard J, Gatti C, Hambley TW (2003) New J Chem 27:1392–1398
22. Duke CB (1996) Chem Rev 96:1237–1259
23. Robinson IK (1998) Acta Cryst A54:772–778
24. Cargnoni F, Gatti C (2001) Theor Chem Acc 105:309–322
25. Cargnoni F, Gatti C, May E, Narducci D (2000) J Chem Phys 112:887–899
26. Gatti C (2007 in press) Solid state applications of QTAIM and the source function: molecular crystals, surfaces, host–guest systems and molecular complexes. In: Matta CF, Boyd R (eds) The quantum theory of atoms in molecules, Chap. 7, Wiley-VCH, Weinheim
27. Cargnoni F, Gatti C, Colombo L (1998) Phys Rev B 57:170–177

28. Bongiorno A, Colombo L, Cargnoni F, Gatti C, Rosati M (2000) Europhys Lett 50:608–614
29. EC 5th Framework Program, Research and Technological Development Program: Competitive and Sustainable Growth, Contract number: G5RD-CT2000–00292
30. Ziman JM (1972) Principles of the Theory of Solids. Cambridge University Press, Cambridge
31. Elliott S (1998) The Physics and Chemistry of Solids. Wiley, New York
32. Blake NP, Latturner S, Bryan JD, Stucky GD, Metiu H (2001) J Chem Phys 115:8060–8073
33. Saunders VR, Dovesi R, Roetti C, Causà M, Harrison NM, Orlando R, Zicovich-Wilson CM (1998) CRYSTAL98, User's Manual, University of Torino, Torino
34. Bertini L, Gatti C, ELTRAP, Electron Transport Properties from the Band Structure (2003), CNR-ISTM, Milano
35. Bertini L, Gatti C (2004) J Chem Phys 121:8983–8989
36. Bertini L, Cargnoni F, Gatti C (2006) A Chemical approach to the first-principles modelling of novel thermoelectric materials. In: Rowe DM (ed) Thermoelectric handbook, Macro to Nano, CRC, Taylor & Francis, Boca Raton, FL, USA, Chap. 7
37. Gatti C, Bertini L, Iversen BB, Blake NP (2003) Chem Eur J 9:4556–4568
38. Cargnoni F, Nishibori E, Rabiller P, Bertini L, Snyder GJ, Christensen M, Gatti C, Iversen BB (2004) Chem Eur J 10:3861–3870
39. Christensen M, Iversen BB, Bertini L, Gatti C, Toprak M, Muhammed M, Nishibori E (2004) J Appl Phys 96:3148–3157
40. Stiewe C, Bertini L, Toprak M, Christensen M, Platzek D, Williams S, Gatti C, Müller, Iversen BB, Muhammed M, Rowe M (2005) J Appl Phys 97:044317
41. Bader RFW, De-Cai F (2005) J Chem Theory Comp (2005) 1:403–414
42. Poater J, Solà M, Bickelhaupt FM (2006) Chem Eur J 12:2902–2905
43. Poater J, Solà M, Bickelhaupt FM (2006) Chem Eur J 12:2889–2895
44. Bader RFW (2006) Chem Eur J 12:2896–2901
45. Silvi B (2002) J Mol Struct 614:3–10
46. Macchi P, Sironi A (2003) Coordination Chem Rev 238–239:383–412
47. Bader RFW (1998) J Phys Chem A 102:7314–7323
48. Fradera X, Austen MA, Bader RFW (1999) J Phys Chem A103:304–314
49. Savin A, Silvi B, Colonna F (1996) Can J Chem 74:1088–1096
50. Gatti C, Cargnoni F, Bertini L (2003) J Comput Chem 24:422–436
51. Gatti C, Bertini L (2004) Acta Cryst A 60:438–449
52. Gatti C, Lasi D (2007) Faraday Discuss, DOI 10.1039/b605404h
53. Gatti C, Cargnoni F (1997) Proceedings III Convegno Nazionale di Informatica Chimica, Napoli, Italy, pp 125–128
54. Katan C, Rabiller P, Lecomte C, Guezo M, Oison V, Souhassou M (2003) J Appl Cryst 36:65–73
55. Rabiller P, Souhassou M, Katan C, Gatti C, Lecomte C (2004) J Phys Chem Solids 65:1951–1955
56. Becke AD, Edgecombe KE (1990) J Chem Phys 92:5397–5403
57. Abramov YA (1997) Acta Cryst A53:264–272
58. Popelier PLA (1994) Chem Phys Lett 228:160–164
59. Gatti C, Fantucci P, Pacchioni G (1987) Theor Chim Acta 72:433–458
60. Giacovazzo C (2002) Fundamentals of crystallography, IUCr texts on crystallography 7, Chap. 1, 2nd edn. Oxford Science Publications, Oxford University Press, Oxford
61. Morse M, Cairns SS (1969) Critical point theory in global analysis and differential geometry. Academic, New York
62. Press WH, Flannery BP, Teukolsky SA, Vetterling WT (1986) Numerical recipes, Cambridge University Press, Cambridge
63. Luaña V, Mori-Sánchez P, Costales A, Blanco MA, Martín Pendás A (2003) J Chem Phys 119:6341–6350
64. Madsen GHK, Blaha P, Schwarz K (2002) J Chem Phys 117:8030–8035
65. Silvi B, Gatti C (2000) J Phys Chem A 104:947–953
66. Luaña V, Costales A, Mori-Sánchez P, Blanco M, Martín Pendás A (2004) Acta Cryst A 60:434–437
67. Hô M, Smith VH, Weaver DF, Gatti C, Sagar RP, Esquivel RO (1998) J Chem Phys 108:5469–5475
68. Keith TA (1993) PhD Thesis, McMaster University, Hamilton, Ontario, Canada
69. Gatti C (1997) P2DCRY97 User's Manual, CNR-ISTM, Milano
70. Iversen BB, Larsen FK, Souhassou M, Takata M (1995) Acta Cryst B 51:580–591
71. Dovesi R, Saunders VR, Roetti C, Orlando R, Zicovich-Wilson CM, Pascale F, Civalleri B, Doll K, Harrison NM, Bush IJ, D'Arco P, Llunell M (2006) CRYSTAL06 User's Manual, University of Torino, Torino
72. Popelier PLA (2001) Theor Chem Acc 105:393–399
73. Mayer I, Salvador P (2004) Chem Phys Lett 383:368–375
74. Koritsanszky TS, Coppens P (2001) Chem Rev 101:1583–1627
75. Coppens P, Iversen BB, Larsen FK (2005) Coord Chem Rev 249:179–195
76. Pisani C (2003) J Mol Struct (Theochem) 621:141–147
77. Dovesi R, Civalleri B, Orlando R, Roetti C, Saunders VR (2005), Rev Comp Chem 21:1–125
78. Coppens P, Volkov A (2004) Acta Cryst A60:357–364
79. Schi∅tt B, Overgaard J, Larsen FK, Iversen BB (2004) Int J Quant Chem 96:23–31
80. Bader RFW, Essén H (1984) J Chem Phys 80:1943–1960
81. Swaminathan S, Craven BM, McMullan RK (1984) Acta Cryst B 40:300–306 and references therein
82. Bader RFW, Larouche A, Gatti C, Carroll MT, MacDougall PJ, Wiberg K (1987) J Chem Phys 87:1142–1152
83. Lunelli B, Roversi P, Ortoleva E, Destro R (1996) J Chem Soc Faraday Trans 92:3611–3623
84. Destro R (1997) Chem Phys Lett 275:463–468
85. Taylor R, Kennard O (1982) J Am Chem Soc 104:5063–5070
86. Steiner T (1997) Chem Commun 727–734
87. Koch U, Popelier PLA (1995) J Phys Chem 99:9747–9754
88. Espinosa E, Molins E, Lecomte C (1998) Chem Phys Lett 285:170–173
89. Espinosa E, Souhassou M, Lachekar H, Lecomte C (1999) Acta Cryst B 55:563–572
90. Espinosa E, Alkorta I, Elguero J, Molins E (2002) J Chem Phys 117:5529–5542
91. Spackman MA (1999) Chem Phys Lett 301:425–429
92. Filler MA, Bent SF (2003) Progr Surf Sci 73:1–56
93. Sakama H, Kawazu A (1995) Mat Sci Eng R14:255–317
94. Mayne AJ, Riedel D, Comtet G, Dujardin G (2006) Progr Surf Sci 81:1–51
95. Feidenhans'l R, Bunk O, Ciston J, Marks LD (2005) Acta Cryst A61:C96
96. Feder R, Mönch W (1984) Solid State Comm 50:311–313
97. Himpsel FJ, Marcus PM, Tromp R, Batra IP, Cook MR, Jona F, Liu H (1984) Phys Rev B30:2257–2259
98. Sakama H, Kawazu A, Ueda K (1986) Phys Rev B34:1367–1370

99. Smit L, Tromp RM, Van Der Veen JF (1985) Surf Sci 163:315–334
100. Himpsel FJ, Heimann P, Eastman DE (1981) Phys Rev B24:2003–2008
101. Uhrberg RIG, Hansson GV, Nichols JM, Flodström SA (1982) Phys Rev Lett 48:1032–1035
102. Martensson P, Cricenti A, Hansson GV (1985) Phys Rev B32:6959–6961
103. Pandey KC (1981) Phys Rev Lett 47:1913–1917
104. Nishiyama A, Terhorst G, Lohmeier M, Molenbroek AM, Frenken JWM (1994) Surf Sci 321:261–266
105. Copel M, Tromp RM, Culbertson RJ (1994) Appl Phys Lett 65:2344–2346
106. Jona F, Thompson WA, Marcus PM (1995) Phys Rev B52:8226–8230
107. Li XP, Vanderbilt D (1992) Phys Rev Lett 69:2543–2546
108. Ancilotto F, Selloni A (1992) Phys Rev Lett 68:2640–2643
109. Blasé X, Zhu X, Louie SG (1994) Phys Rev B 49:4973–4980
110. Van de Walle CG (1994) Phys Rev B49:4579–4585
111. Wolkow RA (1992) Phys Rev Lett 68:2636–2639
112. Felici R, Robinson IK, Ottaviani C, Imperatori P, Eng P, Perfetti P (1997) Surf Sci 375:55–62
113. Lauridsen EM, Baker J, Nielsen M, Feidenhans'l R, Falkenberg G, Bunk I, Zeysing JH, Johnson RL (2000) Surf Sci 453:18–24
114. Boland JJ (1992) Surf Sci 261:17–28
115. Matta CF, Hernández-Trujillo J, Tang T-H, Bader RFW (2003) Chem Eur J 9:1940–1951
116. Tang M, Colombo L, Zhu J, Diaz De La Rubia (1997) Phys Rev B 55:14279–14289
117. Averback RS, Diaz de La Rubia T (1998) Solid State Phys 51:281–402
118. Stich I (1991) Phys Rev B 44:4262–4274
119. Libertino S (1997) Appl Phys Lett 71:389–391
120. DiSalvo FJ (1999) Science 285:703–706
121. Sales BC (2002) Science 295:1248–1249
122. Rowe DM (2006) General Principles and Basic Considerations. In: Rowe DM (ed) Thermoelectrics handbook, macro to nano, CRC Taylor& Francis, Boca Raton, FL, USA, Chap. 1
123. Rowe DM (ed) (2006) Thermoelectrics Handbook, Macro to Nano, CRC Taylor& Francis, Boca Raton, FL, USA, Chaps. 27–42
124. Rogl P (2006) Formation and crystal chemistry of clathrates. In: Rowe DM (ed) Thermoelectrics handbook, macro to nano, CRC Taylor& Francis, Boca Raton, FL, USA, Chap. 32
125. Blake NP, Bryan D, Latturner S, Möllnitz L, Stucky GD, Metiu H (2001) J Chem Phys 114:10063–10074
126. Bentien A, Palmqvist AEC, Bryan JD, Latturner S, Stucky GD, Furenlid L, Iversen BB (2000) Angew Chem Int Ed 39:3613–3616
127. Uher C (2006) General Principles and Basic Considerations. In: Rowe DM (ed) Thermoelectrics handbook, macro to nano, CRC Taylor& Francis, Boca Raton, FL, USA, Chap. 34
128. Nolas GS, Lyon HB, Vohn JL, Tritt TM, Slack GA (1997) In: Proceedings of 16th international conference on thermoelectrics, pp 321–325
129. Sales BC, Chakoumakos BC, Mandrus D (2000) Phys Rev B 61:2475–2481
130. Chen LD, Kawahara T, Tang XF, Goto T, Hirai T, Dyck JS, Chen W, Uher C (2001) J Appl Phys 90:1864–1868
131. Dyck JS, Chen WD, Uher C, Chen L, Tang X, Hirai T (2002) J Appl Phys (2002) 91:3698–3705
132. Wojciechowsky KT (2002) Mat Res Bull 37:2023–2033
133. Bertini L, Billquist K, Christensen M, Gatti C, Holmgren L, Iversen B, Mueller E, Muhammed M, Noriega G, Palmqvist A, Platzek D, Rowe DM, Saramat A, Stiewe C, Toprak M, Williams SG, Zhang Y (2003) Theoretical modeling of Te doped $CoSb_3$. In: Proceedings of the 22nd international conference on thermoelectrics, IEEE Catalog Number 03TH8726, ISBN 0–7803–8301-X, ISSN 1094–2734, pp 85–88
134. Sofo JO, Mahan GD (1998) Phys Rev B 58:15620–15623
135. Kawaharada Y, Kurosaki K, Uno M, Yamanaka S (2001) J Alloy Comp 315:193–197
136. Wojciechowsky KT, Tobola J, Leszczyński J (2003) J Alloys Comp. 361:19–27
137. Cenedese S, Bertini L, Gatti C (2005) In: Proceedings of the ECT 2005, Nancy, France extended abstracts, pp 164–167
138. Cenedese S, Bertini L, Gatti C (2005) In: Proceedings of the ECT 2005, Nancy, France extended abstracts, pp 53–55
139. Bertini L, Stiewe C, Toprak M, Williams S, Platzek D, Zhang Y, Gatti C, Mueller E, Muhammed M, Rowe M (2003) J Appl Phys 93:438–447
140. Fleurial J-P, Caillat T, Borshchevsky A (1997) Proceedings of the XVI international conference on thermoelectrics, Dresden, Germany, August 26–29
141. Watcharapasorn A, DeMattei RC, Feigelson RS, Caillat T, Borshchevsky A, Snyder GJ, Fleurial J-P, Thermoelectric Properties of Some Cobalt Phosphide-Arsenide Compounds. Mat Res Soc Symp 626:Z1.4.1
142. Singh DJ (2000) Semicond Semimetals 70:125–177
143. Caillat T, Fleurial J-P, Borshchevsky (1997) J Phys Chem Solids 58:1119–1125
144. Snyder GJ, Christensen M, Nishibori E, Caillat T, Iversen BB (2004) Nat Mater 3:458–463
145. Kim S-G, Mazin II, Singh DJ (1998) Phys Rev B 57:699–6203
146. Mayer HW, Mikhail I, Schubert K (1978) J Less-Common Met 59:43–52
147. Arfken G (1985) Mathematical methods for physicists, 3rd edn. Academic, Orlando, FL
148. Overgaard J, Schiøtt, Larsen FK, Iversen BB (2001) Chem Eur J 7:3756–3767
149. Farrugia LJ, Evans C, Tegel M (2006) J Phys Chem B 110:7952–7961
150. Jeffrey GA (1997) An introduction to hydrogen bonding, Oxford University Press, New York
151. Gilli G, Gilli P (2000) J Mol Struct 552:1–15
152. Fuster F, Silvi B (2000) Theor Chem Acc 104:13–21
153. Gatti C, Bertini L, Cargnoni F (2005) Acta Cryst A61:C47–C48
154. Cotton FA (2000) J Chem Soc Dalton Trans 1961–1968
155. Llusar R, Beltrán A, Andrés J, Fuster F, Silvi B (2001) J Phys Chem A 105:9460–9466
156. Ponec R, Yuzhakov G, Carbó-Dorca R (2003) J Comput Chem 24:1829–1838
157. Ponec R, Yuzhakov G, Sundberg MR (2005) J Comput Chem 26:447–454
158. Lasi D, Gatti C (2006) European Charge Density Meeting-IV, ECDM-IV, 26–29 January, Branderburg on the Havel, Germany